Title
Application of Linear and Non-Linear Harmonic Methods for Unsteady Transonic Flow

Author
Gundevia, Rayomand

Publication Date
2015

Peer reviewed|Thesis/dissertation

UNIVERSITY OF CALIFORNIA,
IRVINE

Application of Linear and Non-Linear Harmonic Methods for Unsteady Transonic Flow

THESIS

submitted in partial satisfaction of the requirements
for the degree of

MASTER OF SCIENCE

in Mechanical and Aerospace Engineering

by

Rayomand Gundevia

Thesis Committee:
Professor Feng Liu, Chair
Professor Said Elghobashi
Professor Roger Rangel

2015

TABLE OF CONTENTS

LIST OF FIGURES

LIST OF TABLES

ACKNOWLEDGMENTS

I would like to thank Professor Said Elghobashi and Professor Roger Rangel for their help as members of my thesis committee and for their support throughout graduate school at UCI. Without my advisor, Professor Feng Liu, I would not be able to finish this research as he provides both critical advice and insight in a way that is condusive to learning. To my friends in the MAE department and my colleagues of the CFD lab I offer my thanks and hope to continue our friendship in my next steps here at UCI. Finally, I owe a great deal of gratitude for my brother and parents who are always there to guide and support me.

ABSTRACT OF THE THESIS

Application of Linear and Non-Linear Harmonic Methods for Unsteady Transonic Flow

By

Rayomand Gundevia

Master of Science in Mechanical and Aerospace Engineering

University of California, Irvine, 2015

Professor Feng Liu, Chair

This thesis explores linear and non-linear computational methods for solving unsteady flow. The eventual goal is to apply these methods to two-dimensional and three-dimensional flutter predictions. In this study the quasi-one-dimensional nozzle is used as a framework for understanding these methods and their limitations. Subsonic and transonic cases are explored as the back-pressure is forced to oscillate with known amplitude and frequency. A steady harmonic approach is used to solve this unsteady problem for which perturbations are said to be small in comparison to the mean flow. The use of a linearized Euler equations (LEE) scheme is good at capturing the flow characteristics but is limited by accuracy to relatively small amplitude perturbations. The introduction of time-averaged second-order terms in the Non-Linear Harmonic (NLH) method means that a better approximation of the mean-valued solution, upon which the linearization is based, can be made. The nonlinear time-accurate Euler solutions are used for comparison and to establish the regimes of unsteadiness for which these schemes fails. The usefulness of the LEE and NLH methods lie in the gains in computational efficiency over the full equations.

Chapter 1

Introduction

1.1 Problem Summary

In the design stage of aerodynamic surfaces, the ability to run parametric studies is prohibitively costly when time-domain methods are used [1]. Of particular interest is the transonic flutter of wings and turbomachinery blades. For this reason, harmonic perturbation methods are used and allow for most of the non-linear effects to be included in the mean solution and the perturbations while saving computational effort. In order to understand these methods and their limitations, a quasi-1D nozzle study is used. This simplified model serves to provide a way of studying unsteady boundary conditions without the added complexities of geometry.

The outlet back-pressure of the nozzle is forced to oscillate harmonically and this fluctuation is felt in the interior. When the resulting perturbations in the nozzle are small in comparison to the local mean flow, the linearized methods work well in capturing the major unsteady effects. Larger unsteadiness (amplitude or frequency) is handled better by using methods that incorporate more of the non-linear interactions that perturbations and the mean flow

have. These methods are used under the assumption that the unsteady flow-field can be represented by using the first harmonic (perturbations are largely oscillating at the forcing frequency). For subsonic, supersonic, and high frequency transonic flows the linearized theory works well but for lower frequency transonic flows, a range of interest in flutter predictions, this theory breaks down [2]. The inclusion of the non-linear interactions serves to better predict these particular transonic flows.

1.2 Literature Review

1.2.1 Linearized Euler Equations

When the unsteady portion of a flow field is small in comparison to the mean flow, small-perturbation theory can be applied to the Euler equations. Linearizing the Euler equations about a nonlinear mean or steady-state solution is done by using a Taylor expansion and keeping only first-order terms. The use of linearized methods is appropriate only when these first-order terms are the dominant contribution to the unsteady perturbations. Linearized Euler equations (LEE) are used in many computational situations which include the study of wing or blade flutter (aeroelasticity) and noise suppression (aeroacoutics). Although LEE solutions require less computational time than their fully-nonlinear counterparts, these solutions become less accurate as the amount of unsteadiness, both in perturbation amplitude and forced frequency, increases.

Hall [3] studied the Quasi-1D nozzle and used a harmonic LEE method to solve for the first harmonic. With either the back pressure or the inlet pressure varying harmonically, the subsonic and transonic cases for converging-diverging channels were explored. A Newton iteration method was used to solve the LEE and shock fitting was also employed by specifying shock-jump conditions and assuming a harmonic shock motion. Hall concluded that the LEE

approach was valid so long as the square of the unsteadiness, the pressure amplitude in this case, can be deemed insignificant. In spite of this restriction, the LEE do qualitatively demonstrate the non-linear effects that finite perturbations can have on the unsteady flow. Hall [4] later applied the harmonic LEE method to turbomachinery blades and was able to save substantial computational time over time-marching procedures.

Lindquist [5] performed similar work in the study of the unsteady quasi-1D nozzle using a harmonic LEE method. Shock-fitting was used in transonic cases (strong and weak shocks) and the results were compared to shock-capturing methods. The results of the harmonic LEE were very good and in this study the shock-fitting was deemed to give better results for the sharp discontinuities. To address the shortcomings of shock-fitting in two and three dimensions, Lindquist and Giles explored shock-capturing methods for both quasi-1D and constant area ducts [6, 7]. The same unsteady exit conditions were used in this validation. Artificial viscosity terms were added to the LEE and the validity of doing so was done by tracking the motion and shape of the shock-captured discontinuity. Although the discrete shape of the shock changed with its unsteady motion, the integrated pressure force in the nozzle was negligibly affected by this unsteady shape. This integrated pressure force is the equivalent form of lift that would arise on two and three dimensional surfaces. They concluded that shock-capturing with linearized Euler methods can be applied in two and three dimensions without much loss in solution accuracy.

1.2.2 Harmonic Method

The harmonic method involves casting the governing equations into a frequency representation, effectively removing their time dependence and allowing frequency to become a parameter of the equations. This type of method is useful if the solution is expected to be harmonic or periodic in nature which usually occurs when an oscillatory boundary condi-

tion is used. For the LEE, the harmonic method is implemented by assuming a solution form that is harmonic itself, turning the governing equations into steady-state ones with a complex variable form which must be solved for each frequency of interest.

Three examples of harmonic methods are given by the harmonic LEE method, the Non-Linear Harmonic method, and the Harmonic Balance method (grouped by increasing ability to handle non-linearities). The LEE studies [3, 4, 5] mentioned in section 1.2.1 all rely on harmonic LEE methods but only resolve the first harmonic of the solution. The Non-Linear Harmonic (NLH) method, introduced by Ning and He, uses a non-linear representation for the solution but again only resolves the first harmonic content [8]. Compared to a harmonic LEE method, the use of the NLH method better captures the non-linear effects of the perturbations on the mean flow. The limitations for the NLH method arise when the unsteadiness of the solution requires the use of higher harmonics. For this reason Hall [9] applied the Harmonic Balance (HB) technique in which the solution's harmonic content can be varied. By using the HB method not only can the number of harmonics be specified, but the interaction of said harmonics with each other can also be included. This results in the most accurate solution of the three methods outlined but comes at the highest computational cost.

1.2.3 Higher-Order Unsteady Effects

When the level of unsteadiness increases, either through more rapid oscillation or increased amplitude, the linear perturbations are significant enough to have a time-averaged effect on the mean solution. The mean deviates from the steady-state solution and so any linearization based on this solution is actually not representative of the perturbations or the mean. The mean flow is important in engineering applications as it provides a more representative loading in order to predict lift and drag.

The SLiQ method introduced by Giles [10] serves to better resolve the mean flow by using second-order corrections to the steady flow. These are generated by the unsteady perturbations. SLiQ stands for the three steps in the procedure which are the Steady equations, the Linear-perturbation equations, and the Quadratic corrections to the mean flow. Using an asymptotic expansion approach, certain source terms are added to the steady equations. These terms are either linear in second-order perturbations or quadratic in first-order ones. Grouping the linear terms with the steady-state ones defines the mean state and the quadratic source terms (QST) that remain are then analogous to the Reynolds stress terms in turbulent flow modeling. The three steps for this method proceed as follow:

1. Solve the steady-state Euler equations
2. Linearize the flux and the sources
3. Add the corrective QST terms to the steady-state equation and solve for mean

Limitations for the SLiQ method arise from its derivation in which the perturbations are assumed to be small. The accuracy and validity of the asymptotic approach diminishes greatly as the unsteadiness increases and for many applications this is a limiting factor. Most importantly, the SLiQ method does not include the coupled interaction of the perturbations and the mean, a necessity in most aerodynamic applications of interest.

The Non-Linear Harmonic (NLH) method, introduced by Ning and He [8, 11], addresses the short-comings of methods like the SLiQ. It uses as fully coupled approach; the first-order perturbation and mean equation are coupled and iterated simultaneously. This allows the mean flow to be more accurately solved and as a result the perturbations scale appropriately with increasing levels of unsteadiness. The procedure is outlined below:

1. Solve the steady-state equations until convergence.

2. Solve the linearized equations based on the steady state until convergence.

3. Iterate between the mean and first-order (linearized about the mean) equations until convergence.

When this method is executed, there is an increase in computation time over the SLiQ method but the results are more accurate. The shape of both the mean and perturbation, the magnitude of perturbation, and the mean location of perturbation are better predicted. This ability becomes important for transonic flows in which the time-averaged effect is to smear the shock discontinuity even for moderately small levels of unsteadiness.

1.3 Summary of Thesis

A steady-state method for solving the Quasi-1D nozzle problem is explored in the first part of the research. Solutions of both subsonic and transonic nozzles are found by using an explicit finite-volume scheme to discretize the Euler equations. Convergence acceleration is done by using pseudo-time marching. These results provide the base flow-field.

Understanding how to apply these methods is of primary focus and the analysis of the results will be used for this purpose. The full unsteady Euler equations are used to generate periodic solutions for comparison with the linearized solutions. This time domain solution is Fourier transformed into a frequency domain solution. This solution will be used for comparison to the linearized solutions and will show when the linearized approach is no longer valid. In order to capture unsteady effects, second-order terms are incorporated into the scheme via the Non-Linear Harmonic method. Comparison of the solutions from the LEE method, the NLH method, and the full Euler method are made.

Chapter 2

Steady Euler Method

This chapter presents much of the framework used by the other methods including some of the numerical details, the full form of the governing equations, the computational grid, and the method for handling boundary conditions. The steady-state solution is used as the basis for linearization and the initial condition for time-marching and so the steady method is explored first.

2.1 Quasi-1D Euler Equations

The strong conservative form of the quasi-1D Euler equations is given below. The conservative flow variables vector is given by $\vec{W}$, the convective flux is given by $\vec{F}$, and the source term is given as $\vec{S}$. These vectors are expressed in terms of the primitive variables (density, velocity, and pressure) as well as the conserved flow variables. The ratio of the specific heats of the fluid, γ, is taken to be 1.4 throughout. The conserved flow variables are assumed to be independent of each other and provide the basis for linearization. The unsteady equation

is given by

$$\frac{\partial}{\partial t}\int_{\Delta x}\vec{W}dx + \oint_{A}\vec{f}dA = \int_{\Delta x}\vec{S}dx \tag{2.1}$$

where,

$$\vec{W} = \begin{pmatrix} \rho A \\ \rho u A \\ \rho E A \end{pmatrix} = \begin{pmatrix} W_1 \\ W_2 \\ W_3 \end{pmatrix} \tag{2.2}$$

$$\vec{F} = \vec{f}A = \begin{pmatrix} \rho u A \\ (\rho u^2 + p)A \\ \rho u H A \end{pmatrix} = \begin{pmatrix} F_1 \\ F_2 \\ F_3 \end{pmatrix} = \begin{pmatrix} W_2 \\ (\gamma-1)W_3 + \frac{1}{2}(3-\gamma)\frac{(W_2)^2}{W_1} \\ \frac{W_2}{W_1}\left[\gamma W_3 - \frac{1}{2}(\gamma-1)\frac{(W_2)^2}{W_1}\right] \end{pmatrix} \tag{2.3}$$

$$\vec{S} = \begin{pmatrix} 0 \\ p\frac{\partial A}{\partial x} \\ 0 \end{pmatrix} = \begin{pmatrix} S_1 \\ S_2 \\ S_3 \end{pmatrix} = \begin{pmatrix} 0 \\ (\gamma-1)\left[W_3 - \frac{1}{2}\frac{(W_2)^2}{W_1}\right]\frac{1}{A}\frac{\partial A}{\partial x} \\ 0 \end{pmatrix} \tag{2.4}$$

In the derivation of the quasi-1D equations, a source term dependent on the slope of the area variation and the pressure is introduced. This source term is what allows the flow to take on a steady-state, balancing the convective flux term in the equation. This is in contrast to the strict one-dimensional equations that produce trivial steady-state solutions. Because the steady-state solutions are of interest, the first term of equation (2.1) drops out yielding the steady-state form of the equation, given below.

$$\oint_{S}\vec{f}dA = \int_{\Delta x}\vec{S}dx \tag{2.5}$$

It is useful to express all the flow quantities as functions of both the conserved flow variables and of the primitives. The density, velocity, and total energy are given by,

$$\rho = \frac{W_1}{A} \tag{2.6}$$

$$u = \frac{W_2}{W_1} \tag{2.7}$$

$$E = \frac{W_3}{W_1} \tag{2.8}$$

From these the pressure, speed of sound, Mach number, and total enthalpy are defined to be,

$$p = \rho(\gamma - 1)\left(E - \frac{1}{2}u^2\right) = \frac{(\gamma - 1)}{A}\left(W_3 - \frac{1}{2}\frac{W_2^2}{W_1}\right) \tag{2.9}$$

$$a = \sqrt{\frac{\gamma p}{\rho}} = \left[\gamma(\gamma - 1)\left(\frac{W_3}{W_1} - \frac{1}{2}\left(\frac{W_2}{W_1}\right)^2\right)\right]^{\frac{1}{2}} \tag{2.10}$$

$$M = \frac{u}{a} = \left[\gamma(\gamma - 1)\left(\frac{W_3 W_1}{W_2} - \frac{1}{2}\right)\right]^{-\frac{1}{2}} \tag{2.11}$$

$$H = E + \frac{p}{\rho} = \gamma\frac{W_3}{W_1} + (\gamma - 1)\left(\frac{W_2}{W_1}\right)^2 \tag{2.12}$$

2.2 Boundary Conditions

A variation of the non-reflecting boundary conditions proposed by Giles [12] are used in this study. By knowing the characteristic behavior of the flow at the inlet and outlet, the

boundary can be well defined. Linearizing the Euler equations and then solving for the eigenvalues and eigenvectors of the system, shows that information is transferred through waves. The four characteristics correspond with the entropy wave, the vorticity wave, the upstream pressure wave, and the downstream pressure wave. The vorticity and entropy waves travel with the fluid medium and propagate with velocity u. The pressure (acoustic) waves travel at velocities $u - a$ and $u + a$. Considering a mean flow from left to right with velocity u and speed of sound a, the different cases are illustrated below for the inlet and outlet of the nozzle. On the boundaries three primitive variables are enough to fully define the state and in this case density ρ, velocity u, and pressure p are chosen. Figure 2.2 shows the subsonic and supersonic wave speeds which are important for deciding how information propagates at the inlet and outlet. For example, consider a subsonic inlet at which two of the characteristics point to the interior of the nozzle and one points exterior of the nozzle. Specifying two of the primitive variables and extracting the third one from the interior would fully define this subsonic inlet condition. The opposite is true at the subsonic outlet; two characteristics point to the interior and one points to the exterior.

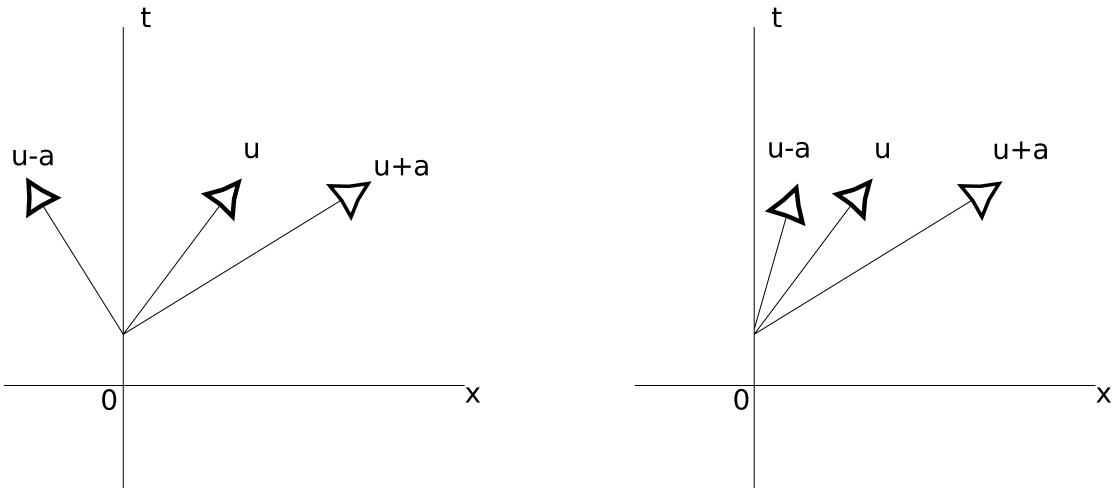

Figure 2.1: A diagram of displacement and time for the characteristic waves of (a) subsonic inlets and (b) supersonic inlets, where the interior domain is given by $x \geq 0$.

At the subsonic inlet, the static density and pressure are prescribed by the following,

$$\rho = \rho_0 \left(1 + \frac{\gamma - 1}{2} M^2\right)^{-\frac{1}{\gamma - 1}} \tag{2.13}$$

$$p = p_0 \left(1 + \frac{\gamma - 1}{2} M^2\right)^{-\frac{\gamma}{\gamma - 1}} \tag{2.14}$$

where the stagnation density and pressure are constants and the Mach number at the inlet is solved iteratively. The quantity W_2 is extrapolated from the interior and serves to provide the condition for velocity here. For the subsonic outlet, the quantities W_1 and W_2 are extrapolated from the interior and serve to provide the conditions for density and velocity. The specified back-pressure provides the last boundary condition at the outlet. The fully subsonic case has a back-pressure ratio of $\frac{p_b}{p_0} = 0.92$ while the transonic case has a back-pressure of $\frac{p_b}{p_0} = 0.75$.

2.3 Numerical Method

The numerical method used in this study is the Jameson-Schmidt-Turkel (JST) scheme [13, 14] which uses a semi-discrete finite-volume scheme to solve the Euler equations. This transformation from fully discrete to semi-discrete form changes the partial differential equation into an ordinary one. For the quasi-1D representation, the semi-discrete scheme takes the following form:

$$\frac{d}{dt}\left(V_j W_j\right) + Q_j = V_j S_j \tag{2.15}$$

For the uniform grid the cell volume (V_j) is given simply as the grid spacing (Δx). The source term (S_j) is evaluated at the cell center while the net flux out of the cell (ΔQ_j) is

approximated at the cell interfaces. The residual of the equation is defined for steady-state convergence as being simply,

$$Res(W_j) = \frac{1}{\Delta x} Q_j - S_j \tag{2.16}$$

Then the simplified equation, when the steady-state application is taken into account, is given by

$$Res(W_j) = 0 \tag{2.17}$$

2.3.1 Convergence Acceleration

The goal for steady-state convergence is to get the residual to tend towards zero. A common convergence acceleration technique is to introduce the so-called pseudo-time forcing term. This forcing term effectively pushes the solution towards the steady state and the solution at each pseudo-time step is representative of a fictitious transient solution. Because only the steady-state result is of interest in this case, the pseudo-time stepping does not have to be time-accurate in nature and must only remain stable. The discretized equation now takes on a pseudo-time dependency (τ) where the superscript n is the index of the previous time-step and $n+1$ the index of the current time-step. In this way the integration is completed explicitly knowing the flow field from the previous time step. Also because the scheme uses explicit time-marching, the non-linear fluxes do not need to be time-linearized as is done for implicit schemes.

$$\frac{d}{d\tau}\left(W_j^{n+1}\right) + Res(W_j^n) = 0 \tag{2.18}$$

Although any time integration scheme can work to time-march this equation, Jameson [15] recommends using multi-stage time integration such as Runge-Kutta schemes. These Runge-Kutta schemes tend to provide more stability than single-stage schemes and also damp out oscillations in the solution between time-steps [16]. This means that larger time steps can be used without the solution diverging. The stability criterion set by the Euler equations is given by the CFL condition below.

$$CFL = (|u_j| + a_j)\frac{\Delta t}{\Delta x} \tag{2.19}$$

This condition sets the maximum time step allowed for the j^{th} cell where the maximum wave speed of the cell is given by $|u_j| + a_j$. The CFL number must be chosen based on the integration scheme being used. For example, the Runge-Kutta (RK) scheme allows for a larger CFL number as compared to single-stage integration and this means that the solution can be advanced at a higher rate (pseudo or real time) for each new time step. Also because this condition is cell-dependent, the time step in each cell can be locally different from neighboring cells. This so-called local time-stepping is used to improve steady-state convergence by allowing the cells that can accommodate larger time steps to do so. This improves the convergence rate because the worst CFL restrictions are isolated to the smallest cells or those that have the highest wave speeds [16]. The general multi-stage setup is given below, where m stages are used. The suggested coefficients (α_i) for the RK 3-stage scheme used in these steady-state calculations, are given as $\alpha = (\frac{2}{3}, \frac{2}{3}, 1)$.

$$\begin{aligned} W^{(0)} &= W^n \\ W^{(i)} &= W^{(0)} - \alpha_i \Delta t Res(W^{(i-1)}) \\ W^{n+1} &= W^{(m)} \end{aligned} \tag{2.20}$$

2.4 Physical Domain

The nozzle geometry used throughout this work is given below as an area variation with respect to axial location. The throat sits at the half-length of the nozzle and the area variation is unique in the convergent and divergent portions.

$$A(x) = \begin{cases} 1 + 1.5\left(1 - \frac{x}{5}\right)^2 & : 0 \leq x \leq \frac{L}{2} \\ 1 + 0.5\left(1 - \frac{x}{5}\right)^2 & : \frac{L}{2} \leq x \leq L \end{cases} \tag{2.21}$$

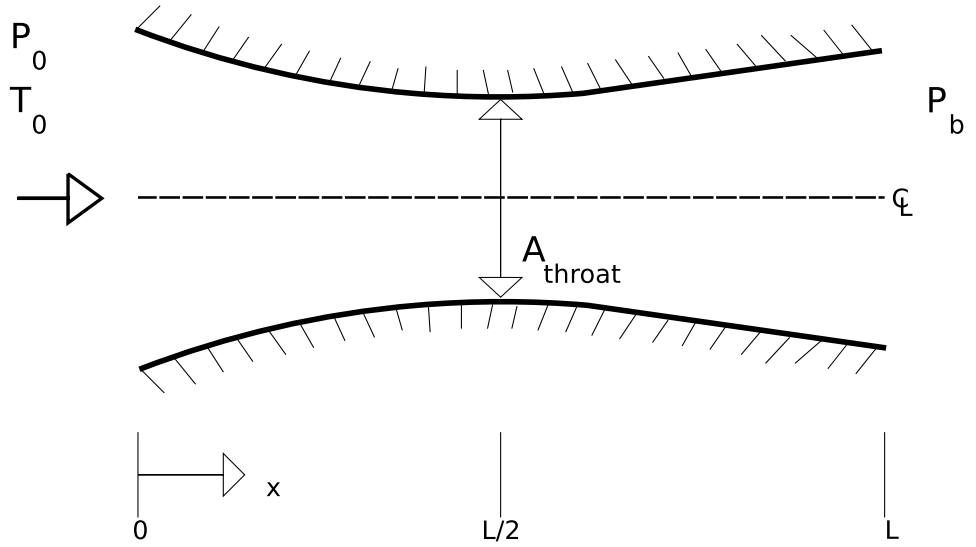

Figure 2.2: A convergent-divergent nozzle with defining geometric characteristics.

2.4.1 Nozzle Grid

The scheme used throughout this thesis is a cell-centered finite-volume one. In the illustration below the j^{th} cell is defined by the cell interfaces $j + \frac{1}{2}$ and $j - \frac{1}{2}$ on either side. At the center of each cell the flow-field is computed and the area specified. The fluxes are evaluated at the interfaces as is consistent with the finite-volume method. The number of cells that define the current computational domain is 200 (201 grid points) where the spacing

is uniform. The accuracy of the solution is dependent on the cell spacing and in this case, under the JST scheme, the accuracy is of second-order.

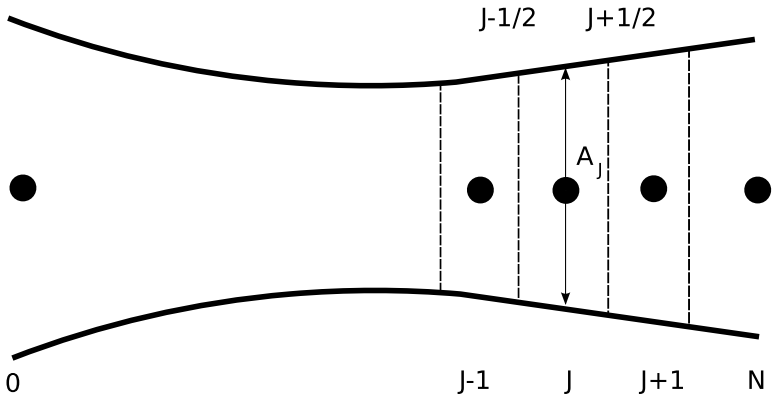

Figure 2.3: This illustration is used to organize the computational indices of the grid.

2.4.2 Flux and Source Terms

The fluxes into or out of a cell are evaluated at the cell's interface. In order to accurately do so, the flow variables must be approximated at the interfaces using the neighboring cell-centered values. On a Cartesian grid this scheme reduces to a finite central-differencing one, where the net flux is expressed using the following:

$$Q_j = F_{j+\frac{1}{2}} - F_{j-\frac{1}{2}} \tag{2.22}$$

The flux at each of the interfaces is given by

$$\begin{aligned} F_{j+\frac{1}{2}} =& \frac{F_j + F_{j+1}}{2} \\ F_{j-\frac{1}{2}} =& \frac{F_j + F_{j-1}}{2} \end{aligned} \tag{2.23}$$

The source term for the momentum equation is directly evaluated (equation (2.4)) using the cell centered values.

$$S_{2j} = (\gamma - 1)\left[W_{3j} - \frac{1}{2}\frac{(W_{2j})^2}{W_{1j}}\right]\frac{1}{A_j}\left(\frac{\partial A}{\partial x}\right)_j \tag{2.24}$$

2.4.3 Artificial Dissipation

The central-difference is consistent with the JST scheme but is not dissipative in nature and spurious oscillations can be triggered, especially by discontinuities in shocked flow [13]. Adding fourth-order dissipation in smooth regions provides nonlinear stability while adding second-order dissipation at discontinuities ensures oscillations are kept to a minimum. The dissipative term added to the semi-discrete equations to make the scheme third-order accurate in smoothly behaving regions and first-order accurate at shocks. This term is given as

$$\frac{d}{dt}(W_j) + \frac{1}{\Delta x}(Q_j - D_j) = S_j \tag{2.25}$$

where the dissipation term is composed of dissipative fluxes given by

$$D_j = d_{j+\frac{1}{2}} - d_{j-\frac{1}{2}} \tag{2.26}$$

The adaptive dissipative flux at each of the interfaces is given by

$$\begin{aligned} d_{j+\frac{1}{2}} =& \epsilon^{(2)}_{j+\frac{1}{2}} R_{j+\frac{1}{2}} \Delta W_j - \epsilon^{(4)}_{j+\frac{1}{2}} R_{j+\frac{1}{2}} \Delta^3 W_j \\ d_{j-\frac{1}{2}} =& \epsilon^{(2)}_{j-\frac{1}{2}} R_{j-\frac{1}{2}} \Delta W_j - \epsilon^{(4)}_{j-\frac{1}{2}} R_{j-\frac{1}{2}} \Delta^3 W_j \end{aligned} \tag{2.27}$$

where $\epsilon^{(2)}$ and $\epsilon^{(4)}$ are adaptive coefficients, R is a scaling coefficient, and ΔW and $\Delta^3 W$ are the first and third differences of W respectively. A shock sensor (ν) is needed in order to

decide when to switch from fourth-order dissipation to second-order dissipation and avoid odd-even point decoupled oscillations. For the $j+\frac{1}{2}$ interface the sensor and coefficients are defined as

$$\nu_j = \frac{|p_{j+1} - 2p_j + p_{j-1}|}{|p_{j+1} + 2p_j + p_{j-1}|} \tag{2.28}$$

$$\epsilon^{(2)}_{j+\frac{1}{2}} = k^{(2)} max\left(\nu_{j+1}, \nu_j\right) \tag{2.29}$$

$$\epsilon^{(4)}_{j+\frac{1}{2}} = max\left(0, k^{(4)} - \epsilon^{(2)}_{j+\frac{1}{2}}\right) \tag{2.30}$$

$$R_{j+\frac{1}{2}} = \frac{\Delta x}{\Delta t} = \frac{\frac{1}{2}\left(|u_j| + a_j + |u_{j+1}| + a_{j+1}\right)}{CFL} \tag{2.31}$$

Typical values for $k^{(2)}$ and $k^{(4)}$ are 1 and $\frac{1}{16}$ respectively.

2.5 Steady-State Results

Residual histories for both subsonic and transonic cases are presented below. Both steady-state solutions used a 3-stage RK scheme with a $CFL = 1.8$. The convergence criterion was set such that the maximum average residual of either continuity, momentum, or energy equations was required to fall below 10^{-9}. The transonic case converges substantially faster (fewer iterations) than the subsonic case and is more smoothly behaving. This can be attributed to the use of second-order dissipation in parts of the transonic field whereas the subsonic field uses only fourth-order dissipation. The difference in orders of dissipation allow for the smearing of perturbations to happen faster. Also another contributing factor for this discrepancy in the convergence rate comes from the physics; the supersonic region (pre-

shock) does not allow for upstream communication and so perturbations are not allowed to propagate upstream in the supersonic region.

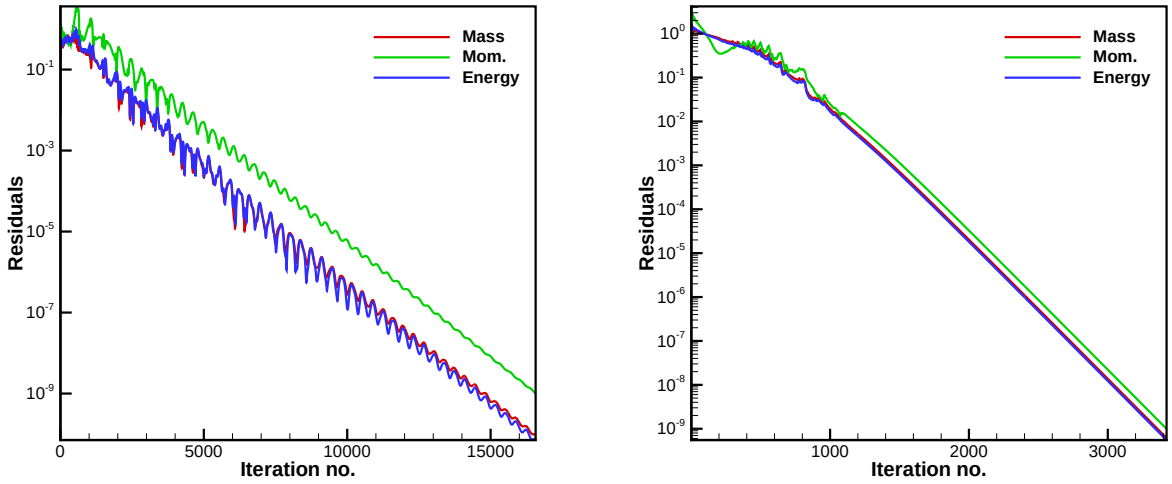

(a) Subsonic (b) Transonic

Figure 2.4: The residual history of the Euler equation.

The following results are the steady-state primitives plotted along the axial direction. The subsonic case has a throat Mach number of 0.6 and is therefore un-choked. The transonic case is choked and the standing shock wave sits at $\frac{x}{L} = 0.86$. Using the JST artificial dissipation has spread the shock across a number of cells but the resemblance to a sharp discontinuity is still there.

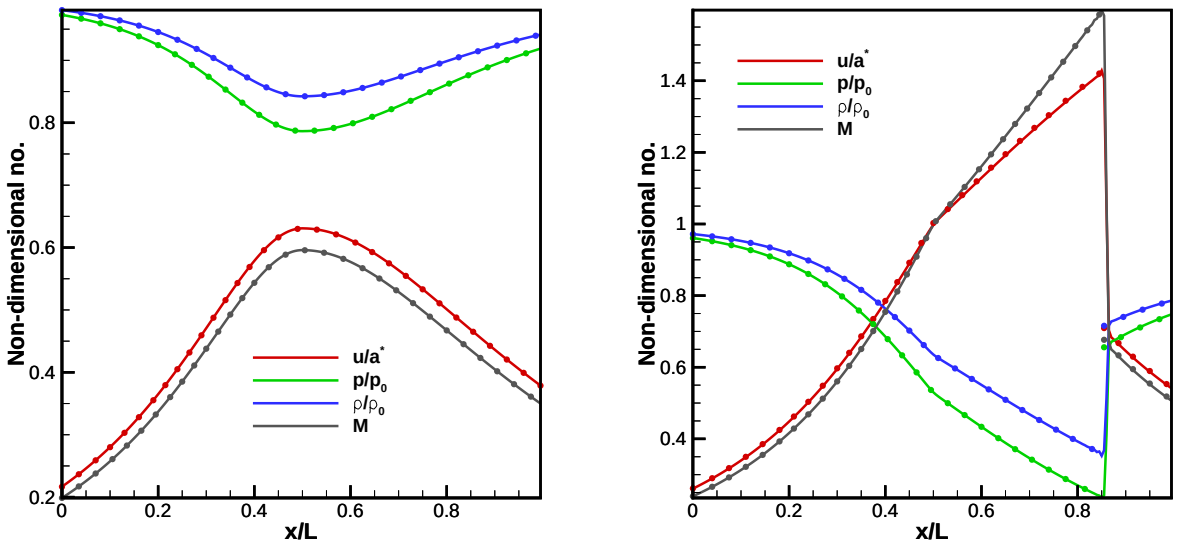

(a) Subsonic

(b) Transonic

Figure 2.5: The non-dimensional quantities of velocity, pressure, density, and Mach number, for both the subsonic and transonic cases, plotting against axial location. The numerical solutions are given by the solid lines and the analytical solutions by the circular symbols.

Chapter 3

Time-Accurate Euler Method

In this thesis the time-accurate method is used as a tool for validation. By comparing the harmonic content from the full Euler solutions to those of the LEE and NLH solutions, an idea of the unsteady behavior and unsteady effects is gained.

3.1 Unsteady Euler Equations

The full Euler equation presented in section 2.1 is used for unsteady flows. The general form that is used is repeated below.

$$\frac{\partial}{\partial t}\int_{\Delta x}\vec{W}dx + \oint_{A}\vec{f}dA = \int_{\Delta x}\vec{S}dx \tag{3.1}$$

3.2 Boundary Conditions

The boundary condition at the inlet remains unchanged from that used in the steady-state chapter. The outlet is harmonically varied as given below.

$$p(L,t) = p_b + \Delta p_b \sin(\omega t) \tag{3.2}$$

where the reduced frequency κ, critical speed of sound a^*, and the nozzle length L are used to specify the oscillation frequency ω.

$$\omega = \frac{\kappa a^*}{L} \tag{3.3}$$

In order to get a sense of the unsteady effects that the boundary condition can impose, both the amplitude of the oscillation and the frequency must be varied. A summary of the specific values used for both κ and $\frac{\Delta p_b}{p_b}$ is given below. The varied reduced frequency groups the results into three cases: 1) the oscillation period is an order of magnitude less than the residence time of the flow, 2) the oscillation period is on the same order as the residence time, and 3) the period is an order greater than the residence time. Also by varying the back pressure amplitude, the effects of higher orders can be explored.

κ:	$\frac{\Delta p_b}{p_b}$:
0.1	0.1%
1.0	0.2%
3.0	0.5%
5.0	1.0%
7.0	2.0%
10.0	5.0%

Table 3.1: The variation of unsteady parameters used in studying both subsonic and transonic flows.

3.3 Initialization

Starting from the steady-state solution, the time-accurate solver is made to run for four or five periods. This ensures that the transient fluctuations have left the flow field and all that remains is the periodic motion of interest. In the two figures below this is illustrated for all the explored cases. The subsonic flows were probed at the throat, a point particularly sensitive to downstream fluctuations. For the reduced frequency of $\kappa = 0.1$ the flow at the throat responds immediately to the back-pressure oscillation. As the reduced frequency is increased, a time lag develops and increases at the throat. Also an increase in oscillation amplitude is presented in a departure from sinusoidal response (especially true at 5%). The transonic cases were probed at the steady-state location of the shock. The square-wave pattern is indicative of an oscillating shock wave. Comparison between the three reduced frequencies reveals that the mean location of the shock varies from the steady-state location. This is indicated by the varied shape of the probed pressure; the sine-like waves don't experience the pressure discontinuity. The transonic cases provides much more departure from sinusoidal form than the subsonic cases.

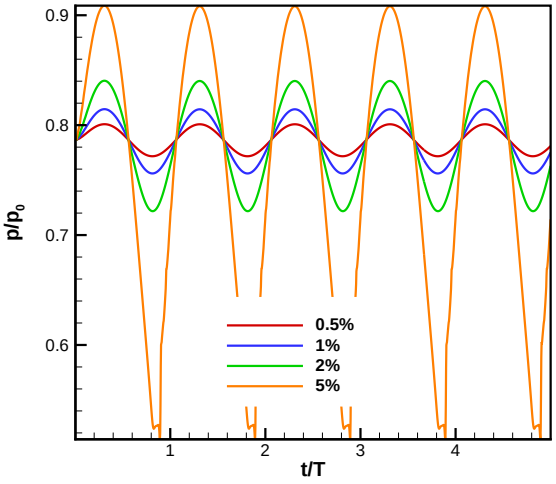

(a) $\kappa = 0.1$

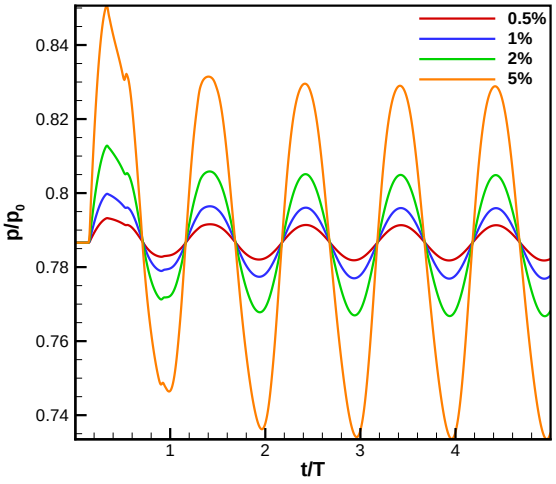

(b) $\kappa = 1.0$

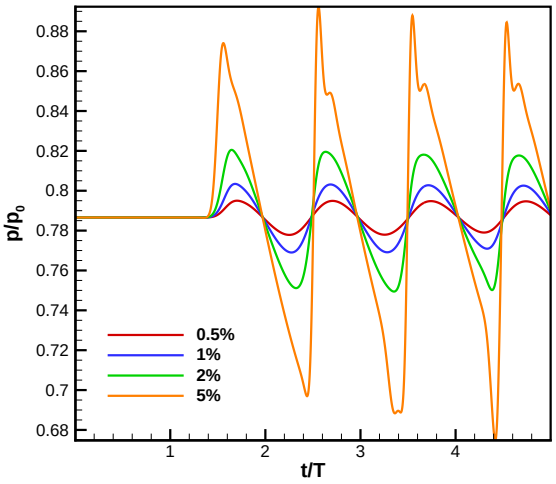

(c) $\kappa = 10.0$

Figure 3.1: Pressure time-history at the throat, subsonic flow.

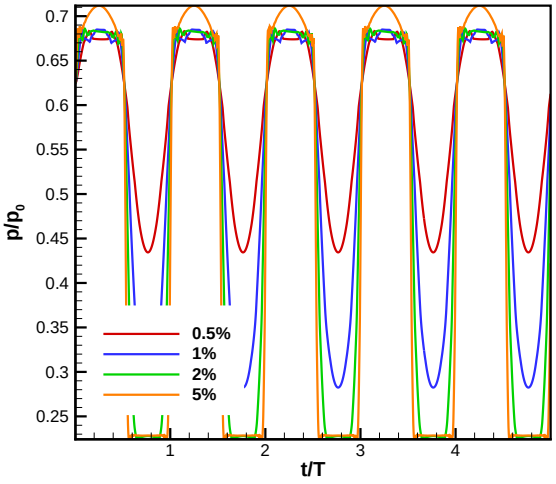

(a) $\kappa = 0.1$

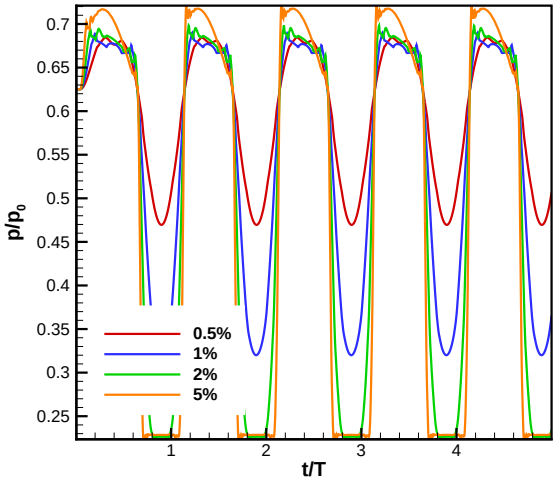

(b) $\kappa = 1.0$

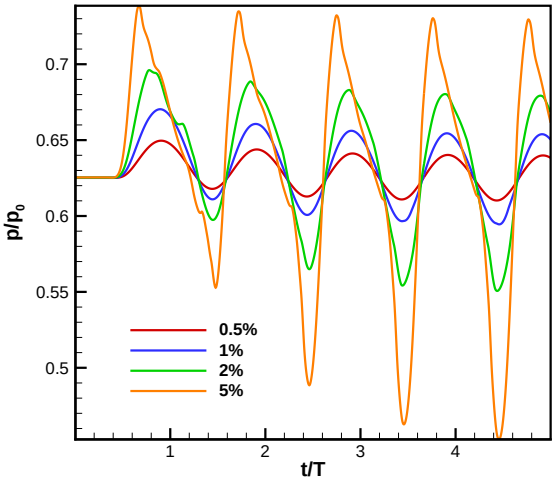

(c) $\kappa = 10.0$

Figure 3.2: Pressure time-history near the steady-state shock location, transonic flow.

3.4 Fourier Analysis

In order to understand the harmonic content of the time-accurate solution, Fourier analysis must be used. Any signal can be decomposed as an infinite summation of trigonometric basis-

functions. The choice of basis function is dependent on whether complex or real coefficients are desired. For example, the unsteady pressure fluctuation is expressed using a complex Fourier series.

$$p'(x,t) = \sum_{-\infty}^{+\infty} {p'}_n(x) e^{i\omega n t} \tag{3.4}$$

Then for each harmonic (represented by n) of the given fundamental frequency (ω), there is a corresponding set of Fourier coefficients (${p'}_n$) that are dependent on the axial location. Because these coefficents are complex numbers, they can be represented as having a real and imaginary part or having an amplitude and a phase angle. The time-harmonic factor ($e^{i\omega n t}$) describes the harmonic variation.

$$\begin{aligned} {p'}_n(x) =& \mathbb{R}\{{p'}_n(x)\} + \mathbb{I}\{{p'}_n(x)\} i \\ =& \hat{p}_n(x) e^{i\phi_n} \end{aligned} \tag{3.5}$$

The phase angle and amplitude are given as,

$$\phi_n = \tan^{-1}\left(\frac{\mathbb{I}\{{p'}_n(x)\}}{\mathbb{R}\{{p'}_n(x)\}}\right) \tag{3.6}$$

$$\hat{p}_n(x) = \sqrt{\mathbb{I}\{{p'}_n(x)\}^2 + \mathbb{R}\{{p'}_n(x)\}^2} \tag{3.7}$$

In order to analyze the discrete solution generated from this time-accurate method, a Fast Fourier Transform (FFT) FORTRAN package is used. FFT fall under the discrete Fourier transforms and are used when a continuous signal is discretized at constant intervals. In order to ensure proper sampling [17], the continuous signal must not contain frequency components that are greater than half of the sampling frequency. This means that if the majority of flow field is expected to respond at the forcing frequency, then the sampling rate

must be at least double that value. However, based on the number of harmonics the flow field is expected to generate the sampling rate must be scaled appropriately.

3.5 Numerical Method

The time-accurate method uses the same JST scheme outlined in chapter 2 but with real-time marching. Because the time-accuracy is important for this method, local time-stepping cannot be performed and instead a global time-step is chosen based on the minimum local time-step. Also because an FFT is to be used, the global time-step must be a constant throughout, ensuring that the data is probed at regular intervals. A conservative estimate of the global time-step must be made such that at subsequent time steps the solution does not become unstable as the flow field changes.

3.6 Time-Accurate Results and Discussion

The following results capture the harmonic content of the flow field for different key cases. The pressure amplitudes for the first, second, and third harmonics are presented to show the contrast in the extremes of back-pressure oscillation. Figure 3.3 shows that in the subsonic case at $\frac{\hat{p}_b}{\Delta p_b} = 5\%$, higher harmonic content is present only for the $\kappa = 10.0$ case and in all cases the first harmonic dominates. In figure 3.4, an interesting flow field develops for the $\kappa = 0.1$ case; during the course of a period of oscillation, a shock appears and disappears. This is evident by looking at the greatly increased gradient near the throat ($x/L = 0.5$) and increase in higher harmonic content when compared to the lower back-pressure case. With the increase in percent back-pressure to 5%, there is a significant increase in higher harmonics with the $\kappa = 10.0$ case no longer dominated by the first harmonic.

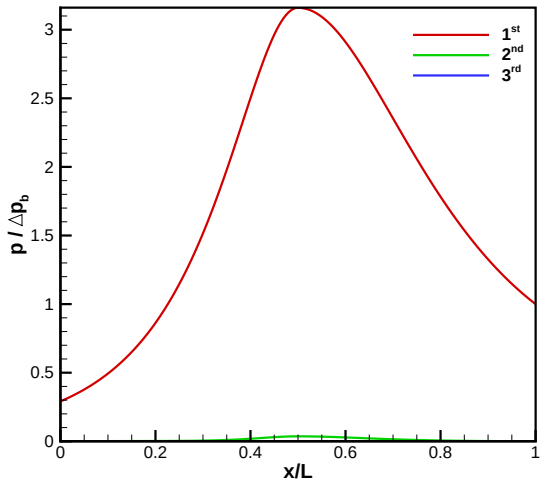

(a) $\kappa = 0.1$

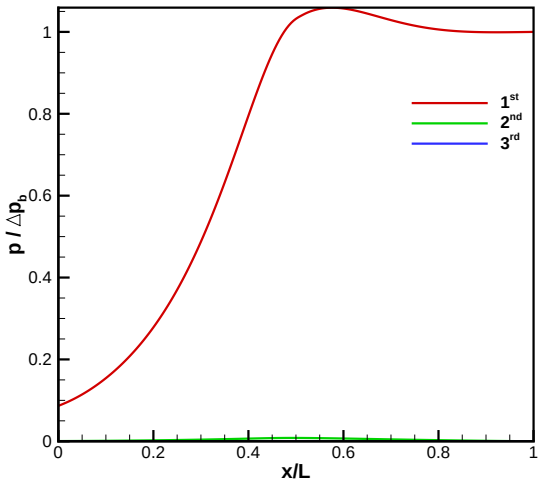

(b) $\kappa = 1.0$

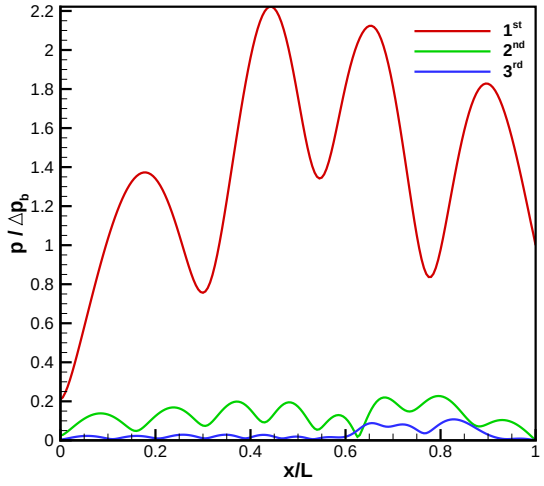

(c) $\kappa = 10.0$

Figure 3.3: Harmonic amplitude at back pressure ratio of 0.5% (subsonic).

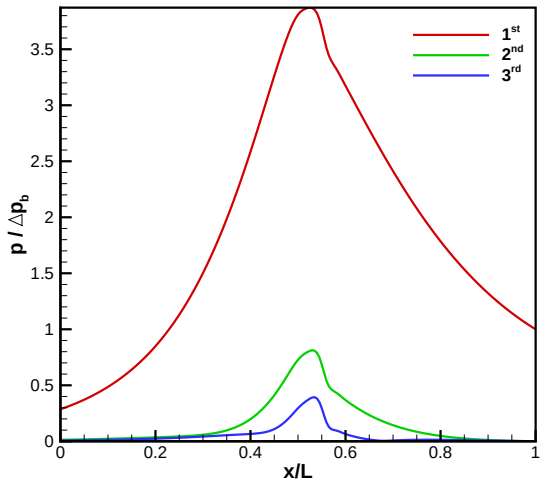

(a) $\kappa = 0.1$

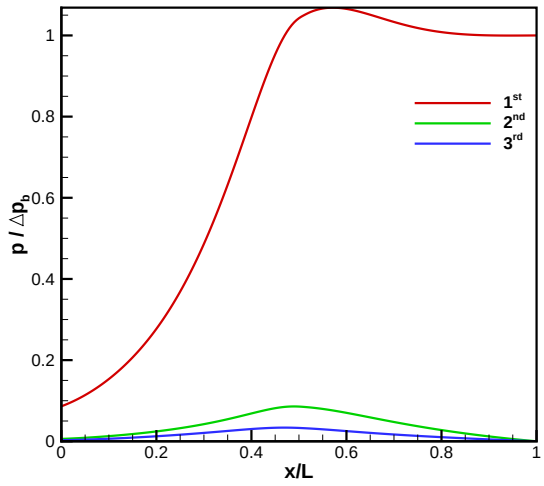

(b) $\kappa = 1.0$

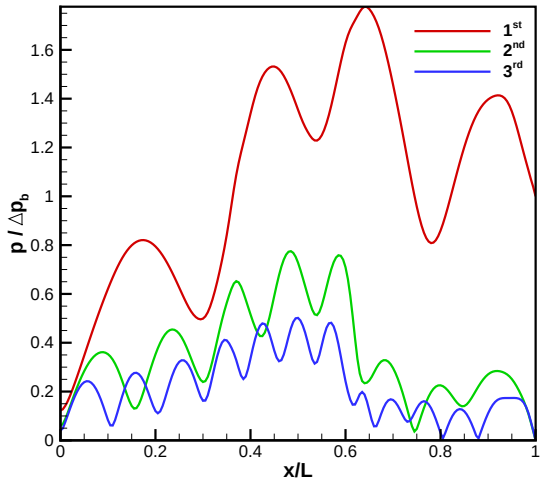

(c) $\kappa = 10.0$

Figure 3.4: Harmonic amplitude at back pressure ratio of 5% (subsonic).

The amplitude plot of a transonic case is given by a large spike centered about the mean location of the shock. For a given pressure change across a shock, an increase in reduced frequency has the effect of reducing the magnitude of this spike. Increasing the back-pressure amplitude has the effect of smearing or spreading the spike. In figure 3.5, there is a resemblance amongst all cases with the higher harmonic content being linked to lower reduced

frequency, a result in contrast to the subsonic case. In figure 3.6, an increase in amplitude has smeared the shock effects over a larger range and has also introduced higher harmonic content. For the $\kappa = 10.0$ case, the overall spike shape has not changed but the amount of higher harmonics has greatly increased.

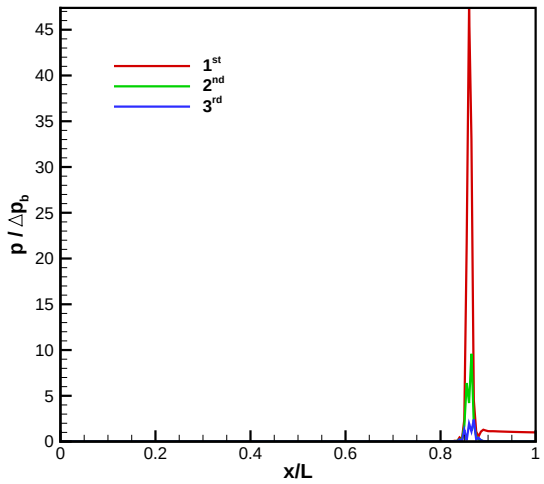

(a) $\kappa = 0.1$

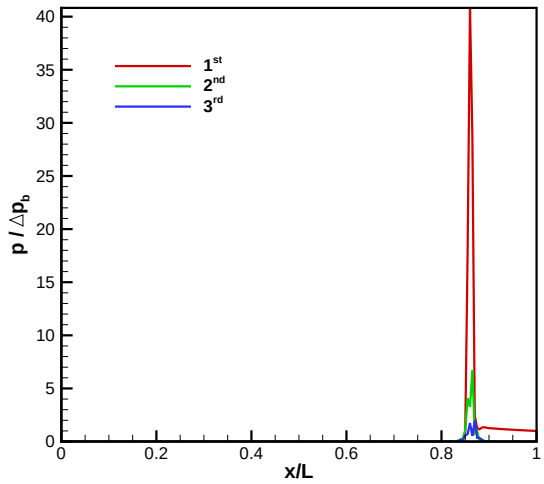

(b) $\kappa = 1.0$

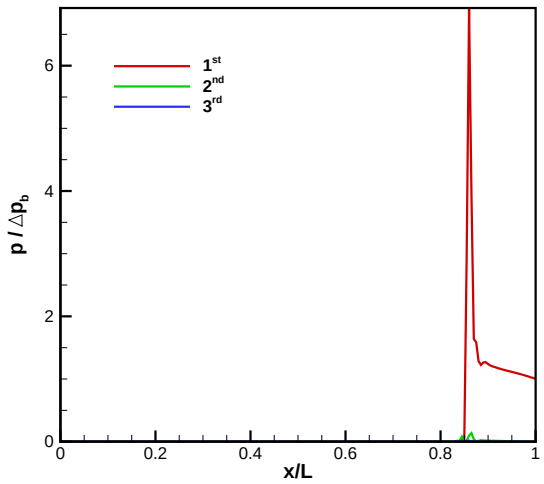

(c) $\kappa = 10.0$

Figure 3.5: Harmonic amplitude at back pressure ratio of 0.5% (transonic).

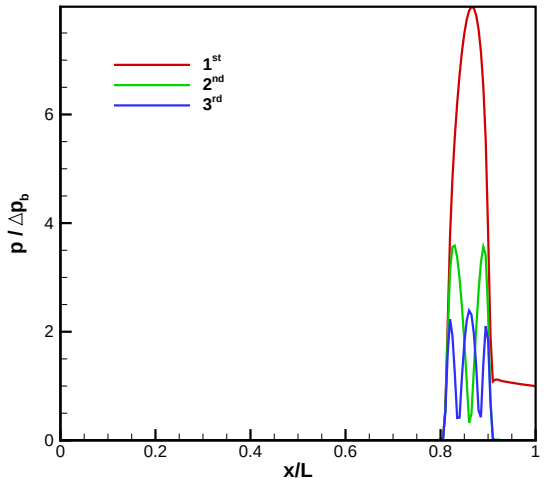

(a) $\kappa = 0.1$

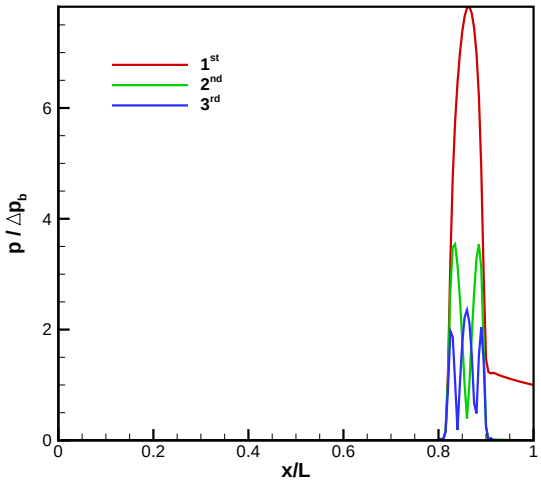

(b) $\kappa = 1.0$

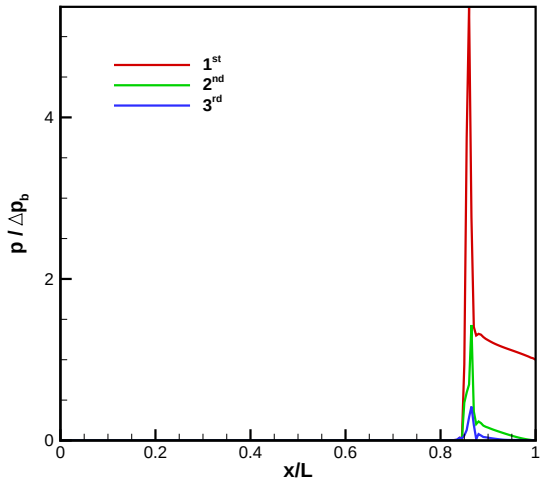

(c) $\kappa = 10.0$

Figure 3.6: Harmonic amplitude at back pressure ratio of 5% (transonic).

Based on the results of the unsteady analysis, the LEE results should be able to represent the subsonic cases without much higher harmonic content (essentially $\kappa = 0.1$ and 1.0). For the transonic cases, the LEE will be able to represent the few cases in which the mean solution does not vary much near the shocked region (compared to the steady-state). The

NLH results should be able to address this problem for these cases because of the non-linear approach.

Chapter 4

Linearized Euler Method

The general procedure for solving the LEE is to first solve the steady-state equations and then find the Jacobian matrices that define the dynamics of the system around this equilibrium point. The LEE are solved in a complex form but still rely on the pseudo-time marching acceleration techniques. This coupled form means that a real and imaginary equation exists for each of the governing equations.

4.1 Linearized Euler Equations

When the perturbation of the flow field is expected to be small, compared to the local mean flow, the governing equations can be linearized about the steady-state flow. It is assumed that the flow field can be composed of a steady value and an unsteady perturbation. This is a standard formulation that is used for aeroelastic problems [18, 19] and will be applied in this work. This same idea is applied to the non-linear terms in the governing equation where the over-bar and over-tilde accents designate steady quantities and unsteady first-order

quantities respectively.

$$W = \overline{W} + \widetilde{W} \tag{4.1}$$

$$f = \overline{f} + \widetilde{f} \tag{4.2}$$

$$S = \overline{S} + \widetilde{S} \tag{4.3}$$

Using the above definitions, the Euler equation becomes

$$\frac{\partial}{\partial t}\int_{\Delta x}\left(\overline{W} + \widetilde{W}\right)dx + \oint_A \left(\overline{f} + \widetilde{f}\right)dA = \int_{\Delta x}\left(\overline{S} + \widetilde{S}\right)dx \tag{4.4}$$

Because this equation has been linearized, the steady-state and perturbation parts can be separated and solved independently of each other. The steady equation has been presented as equation (2.5) and the first-order equation is given as

$$\frac{\partial}{\partial t}\int_{\Delta x}\widetilde{W}dx + \oint_A \widetilde{f}dA = \int_{\Delta x}\widetilde{S}dx \tag{4.5}$$

The non-linear terms are linearized by assuming the following form for the first-order perturbations.

$$\widetilde{f} = \frac{\partial \overline{f}}{\partial \overline{W}}\widetilde{W} = A_f\widetilde{W} \tag{4.6}$$

$$\widetilde{S} = \frac{\partial \overline{S}}{\partial \overline{W}}\widetilde{W} = A_S\widetilde{W} \tag{4.7}$$

where A_f is the convective-flux Jacobian and A_S is the source term Jacobian. The Jacobians are given as

$$A_f = \frac{1}{A}\begin{pmatrix} 0 & 1 & 0 \\ -\frac{1}{2}(3-\gamma)\frac{\overline{W}_2^2}{\overline{W}_1^2} & \frac{1}{2}(3-\gamma)\frac{\overline{W}_2}{\overline{W}_1} & (\gamma-1) \\ \frac{\overline{W}_2}{\overline{W}_1}\left[\frac{1}{2}(\gamma-1)\frac{\overline{W}_2^2}{\overline{W}_1^2} - \gamma\overline{W}_3\right] & \frac{1}{\overline{W}_1}\left[\gamma\overline{W}_3 - \frac{3}{2}(\gamma-1)\frac{\overline{W}_2^2}{\overline{W}_1^2}\right] & \frac{\gamma\overline{W}_2}{\overline{W}_1} \end{pmatrix} \tag{4.8}$$

$$A_S = (\gamma-1)\frac{1}{A}\frac{\partial A}{\partial x}\begin{pmatrix} 0 & 0 & 0 \\ \frac{1}{2}\frac{\overline{W}_2^2}{\overline{W}_1^2} & -\frac{\overline{W}_2}{\overline{W}_1} & 1 \\ 0 & 0 & 0 \end{pmatrix} \tag{4.9}$$

The linearized Euler equation is then given below.

$$\frac{\partial}{\partial t}\int_{\Delta x}\widetilde{W}dx + \oint_A A_f\widetilde{W}dA = \int_{\Delta x} A_S\widetilde{W}dx \tag{4.10}$$

The perturbation is assumed to be harmonic and the first-order solution is given by the following

$$\widetilde{W}(x,t) = \widetilde{W}(x)e^{i\omega t} \tag{4.11}$$

where the complex exponential provides the harmonic variation and complex coefficient $\widetilde{W}(x)$ is given as

$$\widetilde{W} = \widetilde{W}_r + i\widetilde{W}_i = |W|e^{i\phi_W} \tag{4.12}$$

The phase angle of $\widetilde{W}$ is ϕ_W and the amplitude is $|W|$. Applying the solution form from equation (4.11) to the governing equation yields

$$\int_{\Delta x} i\omega\widetilde{W}dx + \oint_A A_f\widetilde{W}dA = \int_{\Delta x} A_S\widetilde{W}dx \tag{4.13}$$

The time dependency has been removed and now the frequency is a parameter of the equation. Because of the complex nature of this equation, it can be split into real parts (subscript r) and imaginary parts (subscript i) given by the following

$$\begin{aligned} -\int_{\Delta x} \omega\widetilde{W}_i dx + \oint_A A_f\widetilde{W}_r dA &= \int_{\Delta x} A_S\widetilde{W}_r dx \\ \int_{\Delta x} \omega\widetilde{W}_r dx + \oint_A A_f\widetilde{W}_i dA &= \int_{\Delta x} A_S\widetilde{W}_i dx \end{aligned} \tag{4.14}$$

where the cross coupling of the equations takes place because of the frequency sources. It should be noted that all quantities presented herein are complex ones and have a form resembling equation (4.12). The primitive variables are also linearized and their perturbations take the following forms

$$\widetilde{\rho} = \frac{1}{A}\widetilde{W}_1 \tag{4.15}$$

$$\widetilde{u} = \frac{1}{\overline{W}_1}\widetilde{W}_2 - \frac{\overline{W}_2}{\overline{W}_1}\widetilde{W}_1 \tag{4.16}$$

$$\widetilde{p} = \frac{(\gamma-1)}{A}\left[\widetilde{W}_3 + \frac{1}{2}\left(\frac{\overline{W}_2^2}{\overline{W}_1^2}\widetilde{W}_1 - \frac{\overline{W}_2}{\overline{W}_1}\widetilde{W}_2\right)\right] \tag{4.17}$$

The linearized forms for the other flow quantities are given below and are expressed using the perturbation of the primitives.

$$\widetilde{E} = \frac{\widetilde{p}}{(\gamma-1)\overline{\rho}} - \frac{\overline{p}\widetilde{\rho}}{(\gamma-1)\overline{\rho}^2} + \overline{u}\widetilde{u} \tag{4.18}$$

$$\widetilde{c} = \frac{1}{2}\left(\frac{\gamma}{\overline{\rho}\overline{p}}\right)^{\frac{1}{2}}\widetilde{p} - \frac{1}{2}\left(\frac{\gamma\overline{p}}{\overline{\rho}^3}\right)^{\frac{1}{2}}\widetilde{\rho} \tag{4.19}$$

$$\widetilde{M} = \frac{\widetilde{u}}{c} - \frac{\overline{u}\widetilde{c}}{c^2} \tag{4.20}$$

$$\widetilde{H} = \widetilde{E} + \frac{\widetilde{p}}{\overline{\rho}} - \frac{\overline{p}\widetilde{\rho}}{\overline{\rho}^2} \tag{4.21}$$

4.2 Boundary Conditions

The linearized boundary conditions for the LEE method are found using the same concepts presented in section 2.2. At the inlet the three quantities that define this boundary are the perturbations in pressure, density, and Mach number. $\widetilde{M}$ is extrapolated from the interior cells and $\widetilde{p}$ and $\widetilde{\rho}$ are specified, knowing that the total pressure and total density have zero fluctuations at the inlet . The perturbations of density and pressure are given by

$$\widetilde{p} = -\frac{\gamma\overline{p}\overline{M}}{1+\frac{\gamma-1}{2}\overline{M}^2}\widetilde{M} \tag{4.22}$$

$$\widetilde{\rho} = -\frac{\overline{\rho}\overline{M}}{1+\frac{\gamma-1}{2}\overline{M}^2}\widetilde{M} \tag{4.23}$$

At the outlet the boundary condition is found by specifying the fluctuation back-pressure and extrapolating $\widetilde{W}_2$ and $\widetilde{W}_1$. For both the inlet and outlet conditions the other primitive variables and flow quantities proceed as given in section 4.1.

4.3 Numerical Method for LEE

The same semi-discrete form of the JST scheme is used for the perturbation equations except now the quantities are complex valued and an additional source term is used. Pseudo-time marching is performed and the real and imaginary equations are solved in a coupled manner. Because the allowable time step is based on the steady-state wave speeds, the CFL number for perturbations of the LEE is lower.

$$\frac{d}{d\tau}(\widetilde{W}_j) + \frac{1}{\Delta x}(\widetilde{Q}_j - \widetilde{D}_j) + i\omega\widetilde{W}_j = \widetilde{S}_j \tag{4.24}$$

$$\frac{d}{d\tau}(\widetilde{W}_j) + Res(\widetilde{W}_j) = 0 \tag{4.25}$$

where the real and imaginary components of the residuals are given as

$$\begin{aligned} Res_r(\widetilde{W}_j) &= \frac{1}{\Delta x}(\widetilde{Q}_{j,r} - \widetilde{D}_{j,r}) - \omega\widetilde{W}_{j,i} - \widetilde{S}_{j,r} \\ Res_i(\widetilde{W}_j) &= \frac{1}{\Delta x}(\widetilde{Q}_{j,i} - \widetilde{D}_{j,i}) + \omega\widetilde{W}_{j,r} - \widetilde{S}_{j,i} \end{aligned} \tag{4.26}$$

For the perturbation equations the JST scheme for artificial dissipation is modified such that the varible coefficients are frozen at their steady-state values. In this way the perturbations of the LEE are subject to the same second-order and fourth-order dissipation terms as before. For the LEE computations, a 3-stage Runge-Kutta integration scheme was used for

the pseudo-time marching. The recommended stage coefficients used are the same as those of the steady-state solver.

4.4 LEE Results and Discussion

The presented results for the LEE method are of the complex pressure-perturbations which are normalized by the back-pressure amplitude. The reduced frequency dictates the shape of the perturbations while the percent back pressure changes the amount of non-linear effects which are included. The LEE perturbations scale with the back pressure because of their linearly assumed form. The extremes in percent back-pressure are used to contrast the effects of increased perturbation amplitude. For comparison the first harmonic of the time-accurate results is plotted alongside the first harmonic generated by the LEE. The convergence history for the real and imaginary mass continuity, conservation of momentum, and conservation of energy are also presented where again the convergence criterion for all residuals was 10^{-9}. Normalized quantities presented include the normalized complex-pressure ($\frac{p'}{\Delta p_b}$) and the normalized residual ($\frac{\frac{1}{N}\Sigma(Res)}{W_{steady}}$).

4.4.1 Subsonic LEE Results

For the subsonic cases, the perturbations of the LEE were solved at a CFL number of 1.0. Overall, the subsonic results are well represented by the LEE except for when non-linearities have significant effects on either the first harmonic or higher harmonics. The time-accurate result in figure 4.2a shows the non-linear behavior that results from the appearance and disappearance of a shock wave, a phenomenon not present in the higher reduced-frequency cases. This case is not suitable for exploration using harmonic methods because the harmonic variation leads to the flow field changing regimes within the span of a single period of oscilla-

tion. Also when the reduced frequency is high, the LEE results show significant errors when compared to the time-accurate results. Figure 4.6 shows that as the back-pressure fluctuation is increased, the first-order solution changes from slightly under predicting the pressure to over predicting it while continuously staying slightly out of phase as well. The nonlinearities and higher harmonics start to play a more significant role for these high reduced-frequencies. Therefore, LEE are not adequate for predicting the harmonic behavior of these higher frequency subsonic cases.

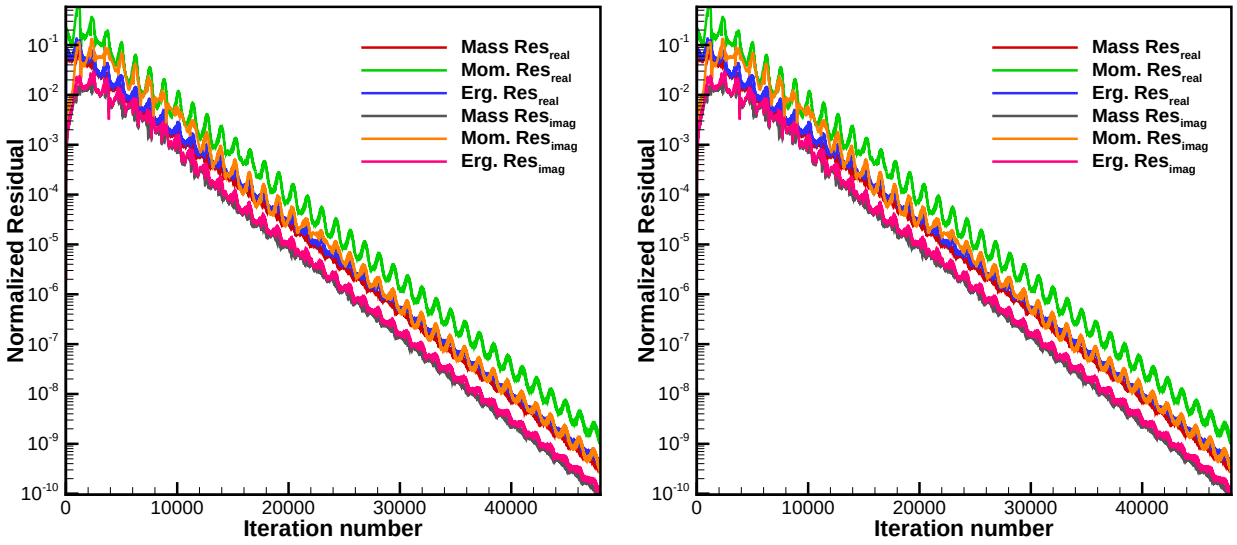

(a) $\frac{\Delta p_b}{p_b} = 0.5\%$ (b) $\frac{\Delta p_b}{p_b} = 5\%$

Figure 4.1: LEE subsonic residual history at $\kappa = 0.1$.

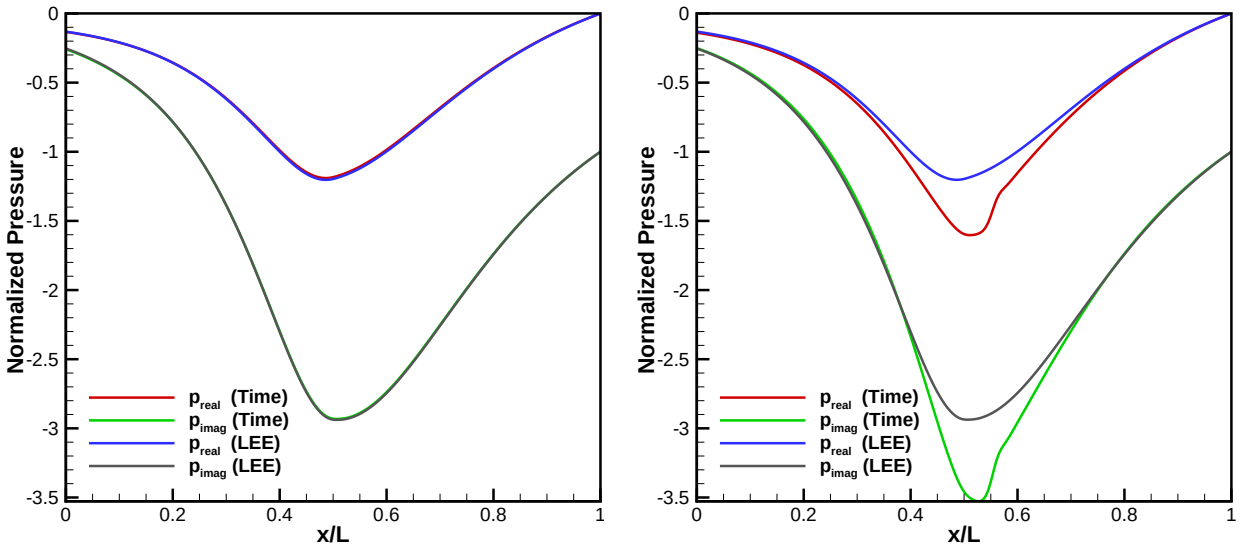

(a) $\frac{\Delta p_b}{p_b} = 0.5\%$ (b) $\frac{\Delta p_b}{p_b} = 5\%$

Figure 4.2: LEE subsonic results for complex pressure at reduced frequency $\kappa = 0.1$.

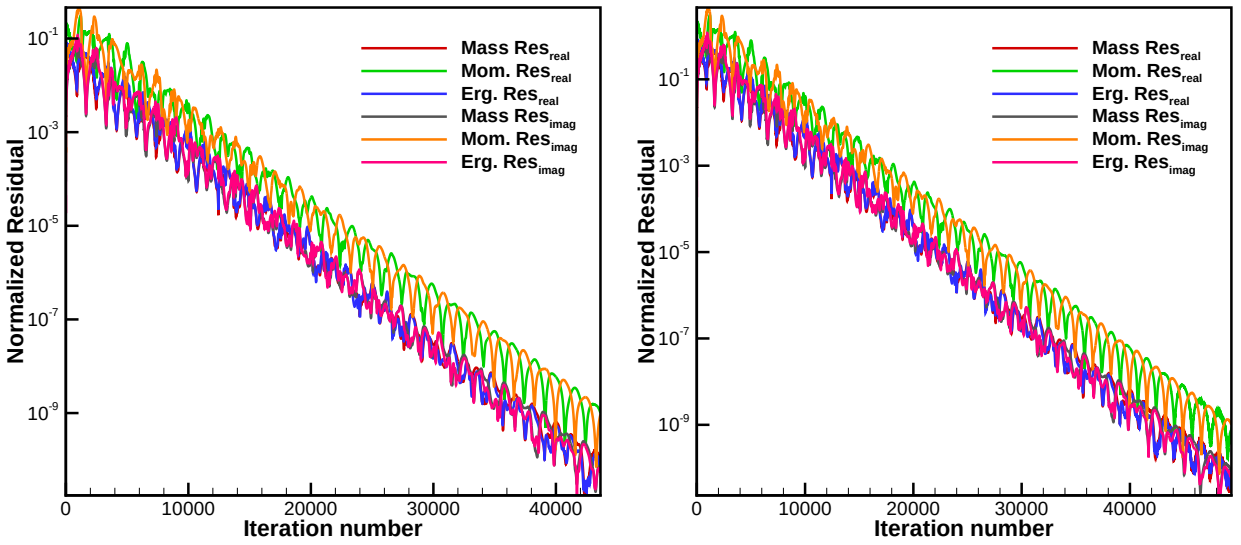

(a) $\frac{\Delta p_b}{p_b} = 0.5\%$ (b) $\frac{\Delta p_b}{p_b} = 5\%$

Figure 4.3: LEE subsonic residual history at $\kappa = 1.0$.

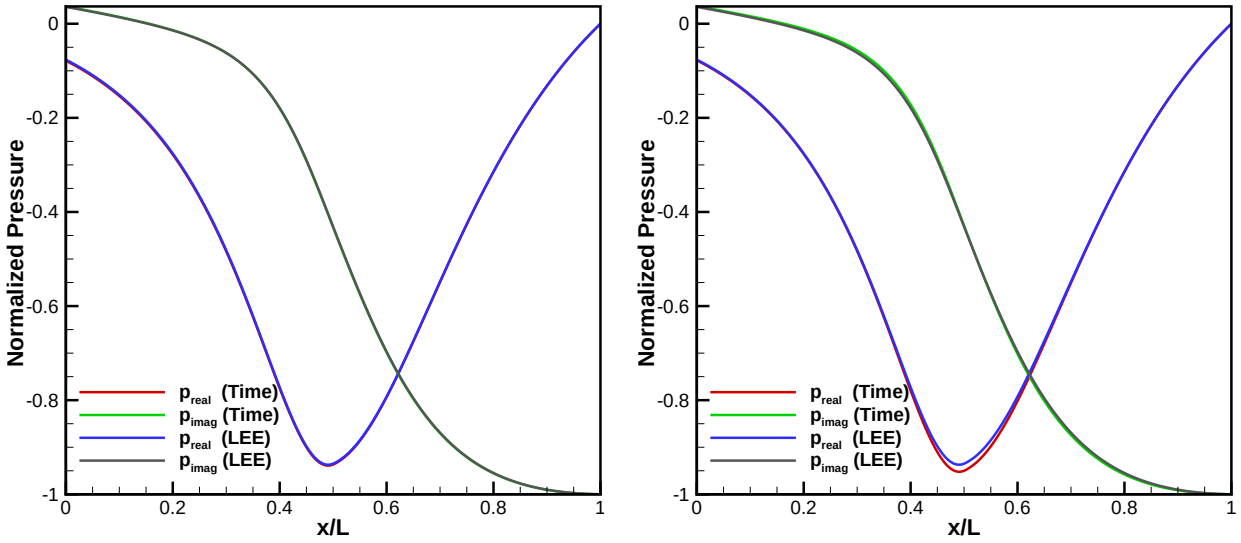

(a) $\frac{\Delta p_b}{p_b} = 0.5\%$ (b) $\frac{\Delta p_b}{p_b} = 5\%$

Figure 4.4: LEE subsonic results for complex pressure at reduced frequency $\kappa = 1.0$.

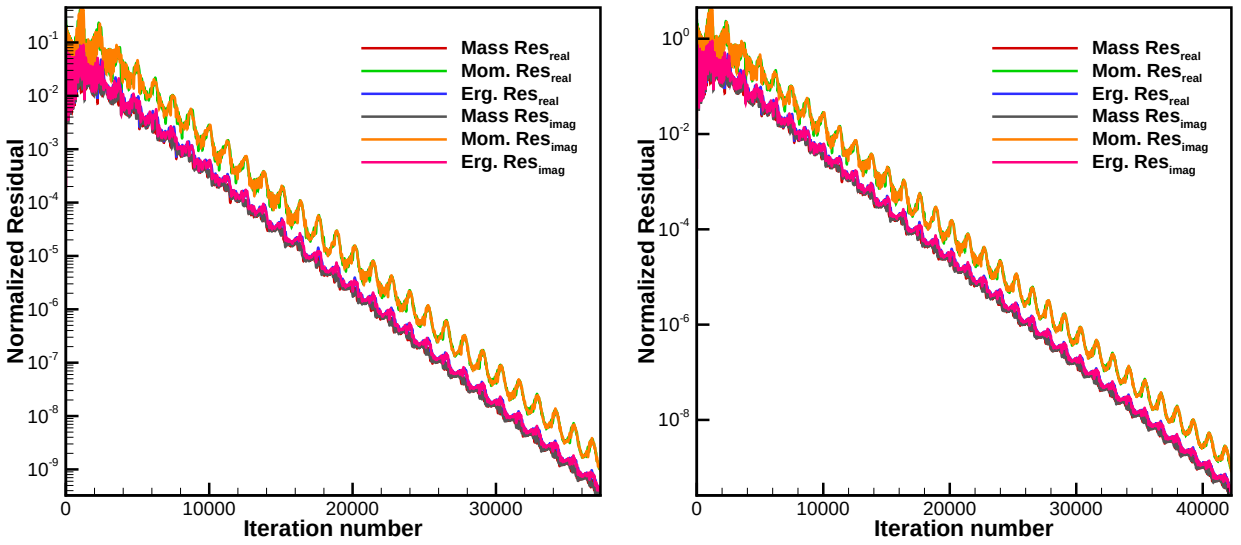

(a) $\frac{\Delta p_b}{p_b} = 0.5\%$ (b) $\frac{\Delta p_b}{p_b} = 5\%$

Figure 4.5: LEE subsonic residual history at $\kappa = 10.0$.

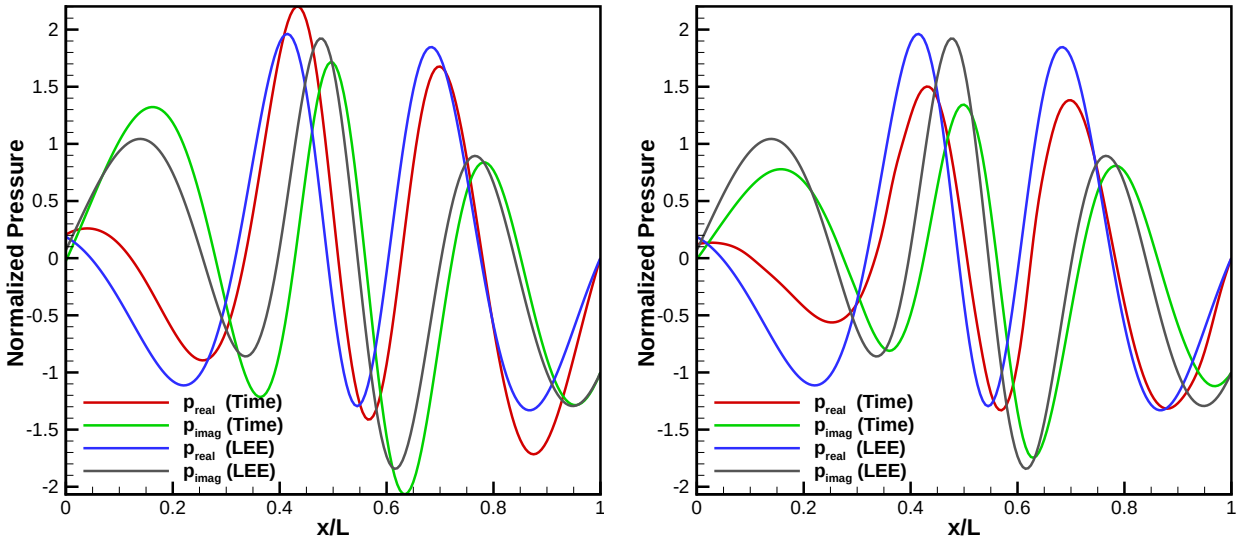

(a) $\frac{\Delta p_b}{p_b} = 0.5\%$ (b) $\frac{\Delta p_b}{p_b} = 5\%$

Figure 4.6: LEE subsonic results for complex pressure at reduced frequency $\kappa = 10.0$.

4.4.2 Transonic LEE Results

The transonic perturbations were solved at a CFL of 0.6. The complex-pressure results below are cropped to show the areas of interest near the shock and downstream of it. These transonic cases present a challenge that is unique; the mean solution of the flow field around the shock can at times be significantly different from the steady-state solution. Because an accurate solution for the mean is not resolved, the LEE method does a poor job of resolving the perturbations for even moderate levels of unsteadiness. Figures 4.7 and 4.8 show this effect. When the back-pressure amplitude is increased the perturbation spike (low amplitude) gets spread out and smeared such that the perturbation covers a larger physical range and also has a smaller maximum amplitude. This effect is missing in the transonic LEE perturbations which, just like the subsonic ones, share a common shape and scale with amplitude. For the higher reduced-frequency case, the trend is that of increased perturbation

accuracy when back-pressure amplitude is increased (see figure 4.9). The first harmonic for this case is adequately predicted because the mean solution is close to the steady-state one. Overall, the LEE alone are not sufficient for predicting the first harmonic at varied levels of unsteadiness for this transonic case.

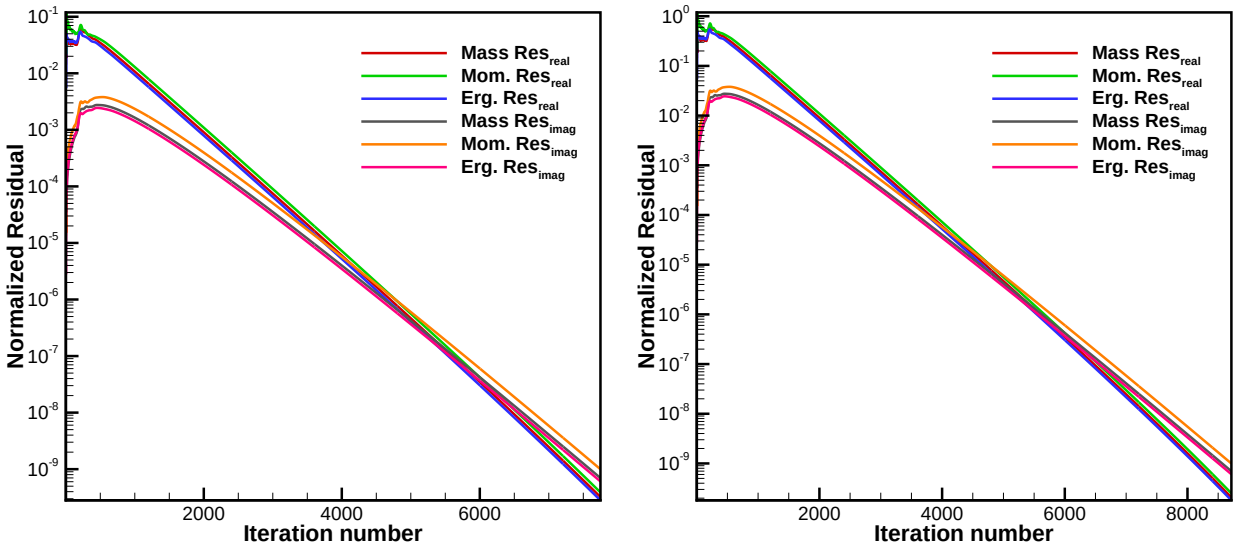

(a) $\frac{\Delta p_b}{p_b} = 0.5\%$ (b) $\frac{\Delta p_b}{p_b} = 5\%$

Figure 4.7: LEE transonic residual history at reduced frequency $\kappa = 0.1$.

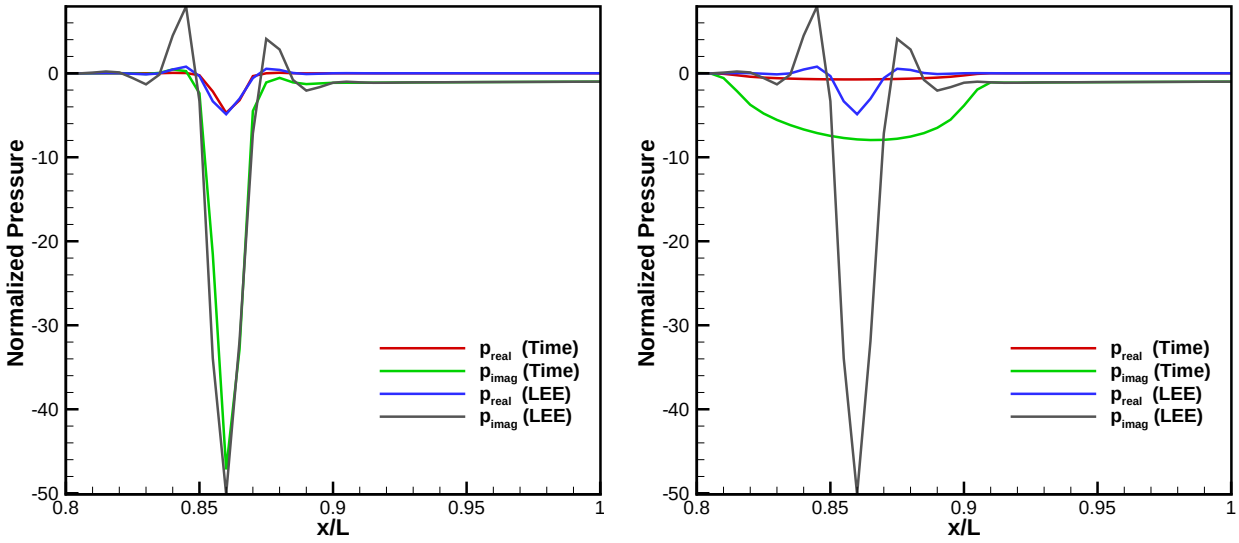

(a) $\frac{\Delta p_b}{p_b} = 0.5\%$ (b) $\frac{\Delta p_b}{p_b} = 5\%$

Figure 4.8: LEE transonic results for complex pressure at reduced frequency $\kappa = 0.1$.

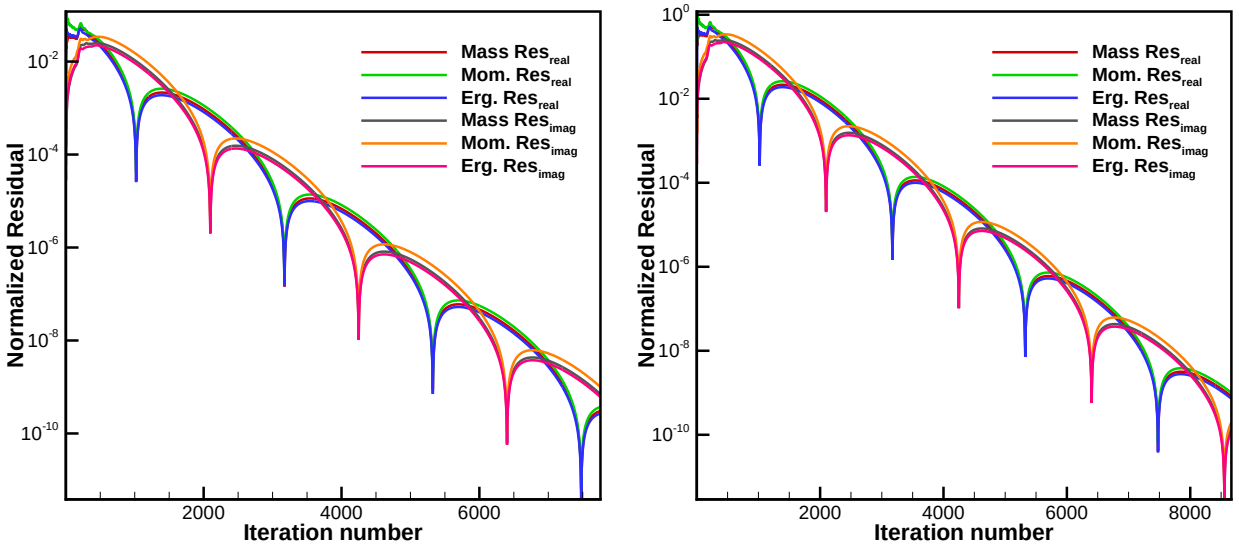

(a) $\frac{\Delta p_b}{p_b} = 0.5\%$ (b) $\frac{\Delta p_b}{p_b} = 5\%$

Figure 4.9: LEE transonic residual history at reduced frequency $\kappa = 1.0$.

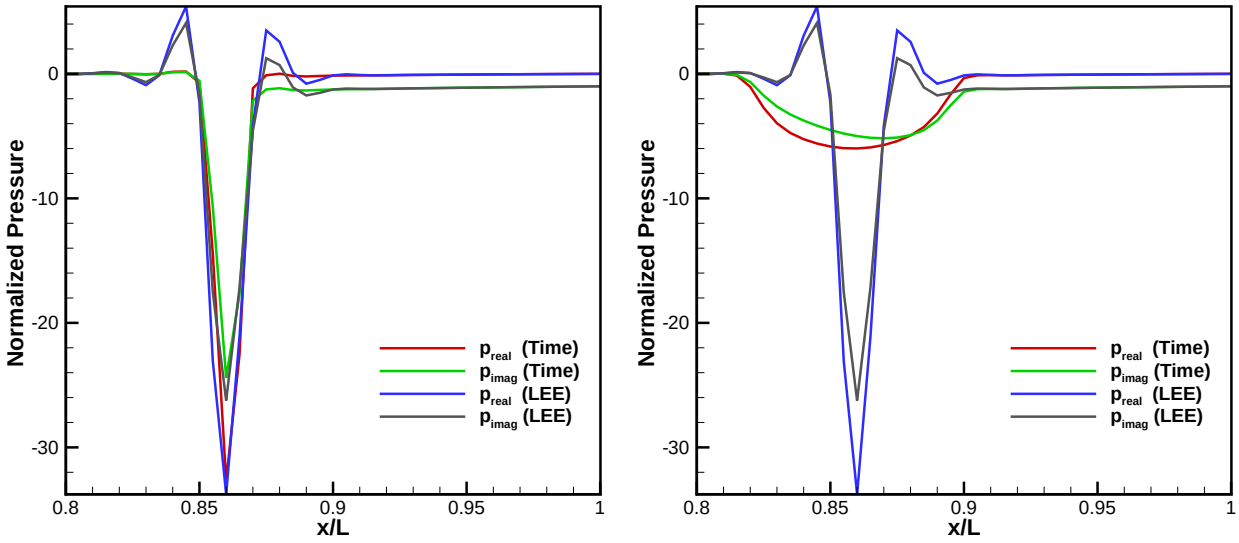

(a) $\frac{\Delta p_b}{p_b} = 0.5\%$ (b) $\frac{\Delta p_b}{p_b} = 5\%$

Figure 4.10: LEE transonic results for complex pressure at reduced frequency $\kappa = 1.0$.

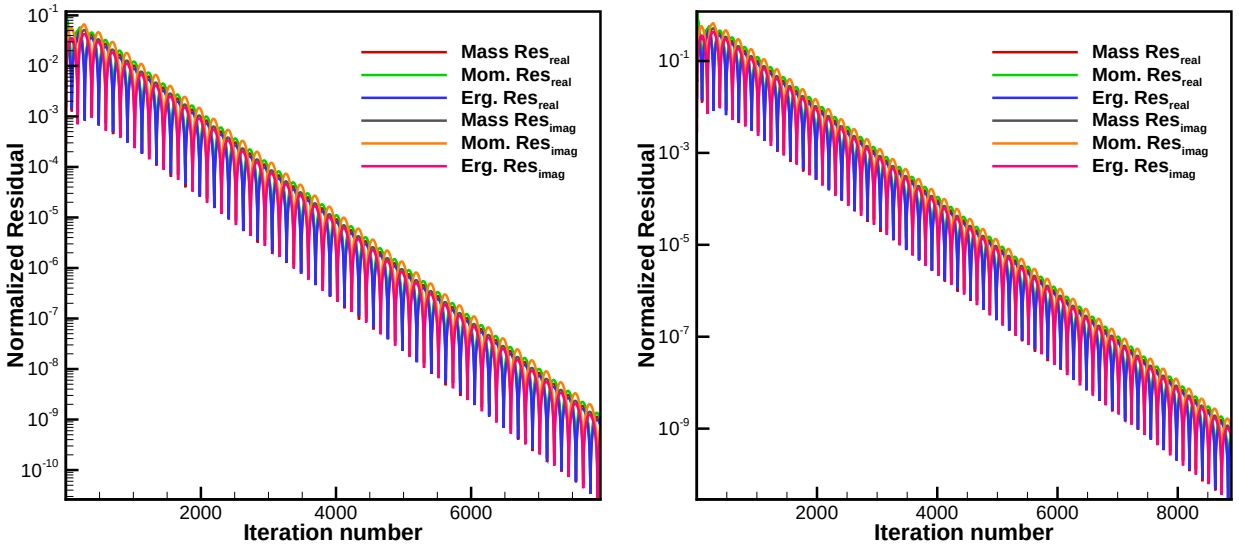

(a) $\frac{\Delta p_b}{p_b} = 0.5\%$ (b) $\frac{\Delta p_b}{p_b} = 5\%$

Figure 4.11: LEE transonic residual history at reduced frequency $\kappa = 10.0$.

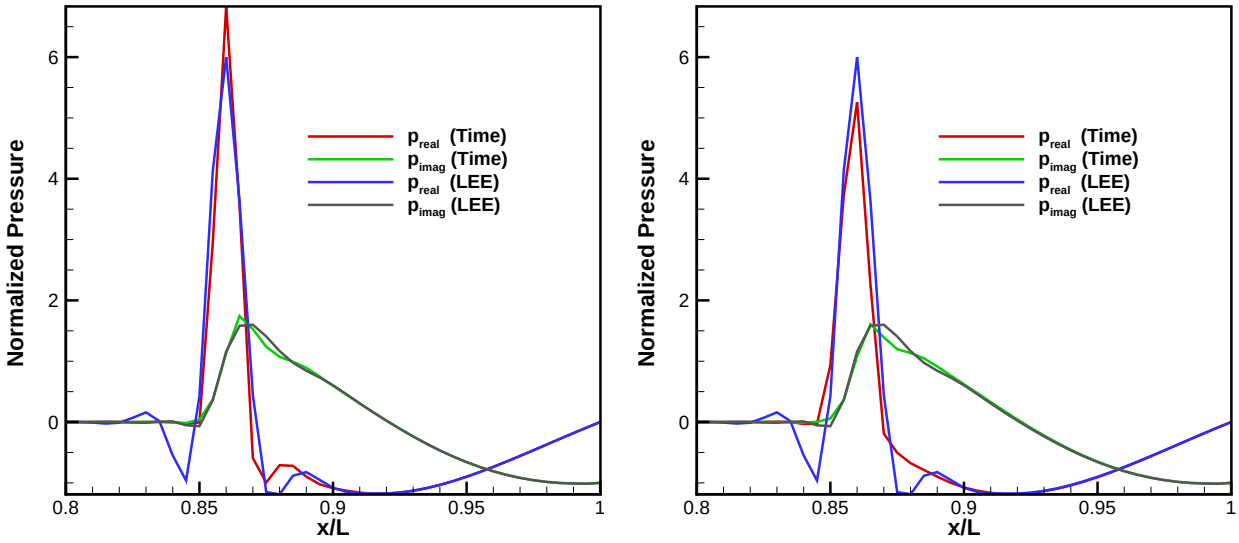

(a) $\frac{\Delta p_b}{p_b} = 0.5\%$ (b) $\frac{\Delta p_b}{p_b} = 5\%$

Figure 4.12: LEE transonic results for complex pressure at reduced frequency $\kappa = 10.0$.

Chapter 5

Non-Linear Harmonic Method

The non-linear harmonic (NLH) method was proposed to deal with accuracy issues when levels of unsteadiness in the flow field cause non-linear effects. The method introduces unsteady stress-like terms analogous to those of the Reynolds-averaged equations [8]. These stress terms are the result of time-averaged perturbation-interactions that develop in the mean equations. Because all terms past the second-order are discarded, the stress terms are all quadratic in perturbations. The time-averaged first-order terms are by definition equal to zero and so it is from the quadratic terms that the mean equations incorporate non-linear interactions.

5.1 Non-Linear Harmonic Equations

The harmonic solution is assumed to have the following form, where an over-bar and over-tilde indicate mean and perturbation quantities respectively,

$$W = \overline{W} + \widetilde{W} \tag{5.1}$$

The convective flux and the source term have the same form given as

$$F_j = \overline{F} + \widetilde{F} \tag{5.2}$$

$$S = \overline{S} + \widetilde{S} \tag{5.3}$$

The non-linear terms of the Euler equations are expanded by substituting equation (5.1) for W. After this substitution is made the equations are time-averaged and then all terms higher than second-order are discarded in order to form the mean-valued equations. The continuity equation is considered first and the mean mass-flux is given as

$$\overline{F}_1 = \oint_A \overline{f}_1 dA = \overline{\overline{W}_2 + \widetilde{W}_2} = \overline{W}_2 \tag{5.4}$$

Then the mean continuity equation has the following form

$$\oint d\overline{F}_1 = 0 \tag{5.5}$$

The mean momentum-flux is given by

$$\begin{aligned} \overline{F}_2 = \oint_A \overline{f}_2 dA &= (\gamma - 1)\overline{\left(\overline{W}_3 + \widetilde{W}_3\right)} + \frac{1}{2}(3-\gamma)\frac{\overline{\left(\overline{W}_2 + \widetilde{W}_2\right)^2}}{\overline{W}_1 + \widetilde{W}_1} \\ &= (\gamma - 1)\overline{W}_3 + \frac{1}{2}(3-\gamma)\left(\frac{\overline{W}_2^2}{\overline{W}_1} + \frac{\overline{W}_2^2}{\overline{W}_1^3}\overline{\widetilde{W}_1^2} - 2\frac{\overline{W}_2}{\overline{W}_1^2}\overline{\widetilde{W}_1\widetilde{W}_2} + \frac{1}{\overline{W}_1}\overline{\widetilde{W}_2^2}\right) \end{aligned} \tag{5.6}$$

which can be broken into the sum of a steady component $F_2^{(0)}$ and a stress term $\widetilde{\overline{F}}_2$. This stress term is simply

$$\widetilde{\overline{F}}_2 = \frac{1}{2}(3-\gamma)\left(\frac{\overline{W}_2^2}{\overline{W}_1^3}\overline{\widetilde{W}_1^2} - 2\frac{\overline{W}_2}{\overline{W}_1^2}\overline{\widetilde{W}_1\widetilde{W}_2} + \frac{1}{\overline{W}_1}\overline{\widetilde{W}_2^2}\right) \tag{5.7}$$

The momentum source term is given as

$$\begin{aligned}\overline{S}_2 =&(\gamma-1)\frac{1}{A}\frac{\partial A}{\partial x}\left[\overline{\overline{W}_3+\widetilde{W}_3} - \frac{1}{2}\overline{\frac{(\overline{W}_2+\widetilde{W}_2)^2}{\overline{W}_1+\widetilde{W}_1}}\right] \\ =&(\gamma-1)\frac{1}{A}\frac{\partial A}{\partial x}\left[\overline{W}_3 - \frac{1}{2}\left(\frac{\overline{W}_2^2}{\overline{W}_1} + \frac{\overline{W}_2^2}{\overline{W}_1^3}\overline{\widetilde{W}_1^2} - 2\frac{\overline{W}_2}{\overline{W}_1^2}\overline{\widetilde{W}_1\widetilde{W}_2} + \frac{1}{\overline{W}_1}\overline{\widetilde{W}_2^2}\right)\right]\end{aligned} \tag{5.8}$$

where the stress term that is introduced by the source, $\widetilde{\overline{S}}_2$, is given as

$$\widetilde{\overline{S}}_2 = -\frac{1}{A}\frac{\partial A}{\partial x}\left(\frac{\gamma-1}{2}\right)\left(\frac{\overline{W}_2^2}{\overline{W}_1^3}\overline{\widetilde{W}_1^2} - 2\frac{\overline{W}_2}{\overline{W}_1^2}\overline{\widetilde{W}_1\widetilde{W}_2} + \frac{1}{\overline{W}_1}\overline{\widetilde{W}_2^2}\right) \tag{5.9}$$

Then the mean momentum equation is given as

$$\oint d\overline{F}_2 = \overline{S}_2 \tag{5.10}$$

The mean energy-flux is given as

$$\overline{F}_3 = \oint_A \overline{f}_3 dA = \overline{\frac{\gamma(\overline{W}_2 + \widetilde{W}_2)(\overline{W}_3 + \widetilde{W}_3)}{\overline{W}_1 + \widetilde{W}_1}} - \frac{1}{2}(\gamma - 1)\overline{\frac{(\overline{W}_3 + \widetilde{W}_3)^3}{(\overline{W}_1 + \widetilde{W}_1)^2}}$$

$$\begin{aligned} =&\gamma \left[\frac{\overline{W}_2 \overline{W}_3}{\overline{W}_1} + \frac{\overline{W}_2 \overline{W}_3}{\overline{W}_3^3} \overline{\widetilde{W}_1^2} - \frac{\overline{W}_2}{\overline{W}_1^2} \overline{\widetilde{W}_1 \widetilde{W}_3} - \frac{\overline{W}_3}{\overline{W}_1^2} \overline{\widetilde{W}_1 \widetilde{W}_2} + \frac{1}{\overline{W}_1} \overline{\widetilde{W}_1^2} \right] \\ &- \frac{1}{2}(\gamma - 1) \left[\frac{\overline{W}_2^3}{\overline{W}_2^2} + 3\frac{\overline{W}_2^3}{\overline{W}_1^4} \overline{\widetilde{W}_1^2} - 6\frac{\overline{W}_2^2}{\overline{W}_1^3} \overline{\widetilde{W}_1 \widetilde{W}_2} + 3\frac{\overline{W}_2}{\overline{W}_1^2} \overline{\widetilde{W}_2^2} \right] \end{aligned} \tag{5.11}$$

where the stress term introduced by the energy flux, $\widetilde{\overline{F}}_3$, is given as

$$\begin{aligned} \widetilde{\overline{F}}_3 =&\gamma \left[\frac{\overline{W}_2 \overline{W}_3}{\overline{W}_3^3} \overline{\widetilde{W}_1^2} - \frac{\overline{W}_2}{\overline{W}_1^2} \overline{\widetilde{W}_1 \widetilde{W}_3} - \frac{\overline{W}_3}{\overline{W}_1^2} \overline{\widetilde{W}_1 \widetilde{W}_2} + \frac{1}{\overline{W}_1} \overline{\widetilde{W}_1^2} \right] \\ &- \frac{1}{2}(\gamma - 1) \left[3\frac{\overline{W}_2^3}{\overline{W}_1^4} \overline{\widetilde{W}_1^2} - 6\frac{\overline{W}_2^2}{\overline{W}_1^3} \overline{\widetilde{W}_1 \widetilde{W}_2} + 3\frac{\overline{W}_2}{\overline{W}_1^2} \overline{\widetilde{W}_2^2} \right] \end{aligned} \tag{5.12}$$

The mean energy-equation is given as

$$\oint d\overline{F}_3 = 0 \tag{5.13}$$

The mean-valued primitive variables are found in a similar way; the quantity is expanded using equation (5.1) and then time-averaged. The mean density is given as

$$\overline{\rho} = \frac{\overline{W}_1}{A} \tag{5.14}$$

The following defines the mean velocity

$$\overline{u} = \frac{\overline{W}_2 - \overline{\widetilde{\rho}\widetilde{u}}A}{\overline{\rho}A} \tag{5.15}$$

while the mean pressure is given by

$$\overline{p} = (\gamma - 1)\left[\frac{\overline{W}_3}{A} - \frac{1}{2}\left(\overline{\rho}\overline{u}^2 + 2\overline{u}\overline{\widetilde{\rho}\widetilde{u}}\right)\right] \tag{5.16}$$

The mean values of the total energy, speed of sound, Mach number, and total enthalpy are found using the mean primitives and their time-averaged products.

$$\overline{E} = \frac{1}{\overline{\rho}}\left(\frac{\overline{W}_3}{A} - \overline{\widetilde{\rho}\widetilde{E}}\right) \tag{5.17}$$

$$\overline{a} = \gamma^{\frac{1}{2}}\left[\left(\frac{\overline{p}}{\overline{\rho}}\right)^{\frac{1}{2}} + \frac{3}{8}\left(\frac{\overline{p}}{\overline{\rho}^5}\right)^{\frac{1}{2}}\overline{\widetilde{\rho}^2} + \frac{1}{4}\left(\frac{1}{\overline{p}\overline{\rho}^3}\right)^{\frac{1}{2}}\overline{\widetilde{\rho}\widetilde{p}} - \frac{1}{8}\left(\frac{1}{\overline{\rho}\overline{p}^3}\right)^{\frac{1}{2}}\overline{\widetilde{p}^2}\right] \tag{5.18}$$

$$\overline{M} = \frac{\overline{u}}{\overline{a}} - \frac{1}{\overline{a}^2}\overline{\widetilde{u}\widetilde{a}} + \frac{\overline{u}}{\overline{a}^3}\overline{\widetilde{a}^2} \tag{5.19}$$

$$\overline{H} = \frac{\overline{p}}{\overline{\rho}} + \overline{E} - \frac{1}{\overline{\rho}^2}\overline{\widetilde{\rho}\widetilde{p}} + \frac{\overline{p}}{\overline{\rho}^3}\overline{\widetilde{\rho}^2} \tag{5.20}$$

In order to evaluate the so-called stress terms, a correlation between perturbations must be established. Because of the assumed harmonic form, the time-averaged products of perturbation quantities can be formulated using the following where it is assumed that the amplitude and phase of the perturbations are known quantities.

$$\begin{aligned}
\overline{\widetilde{W}_m\widetilde{W}_k} =& \frac{1}{T}\int_0^T \widetilde{W}_m e^{i\omega t}\widetilde{W}_k e^{i\omega t}dt \\
=& \frac{1}{T}\int_0^T |W_m|e^{i(\omega t+\phi_m)}|W_k|e^{i(\omega t+\phi_k)}dt \\
=& \frac{1}{2}|W_m||W_k|\cos(\phi_m - \phi_k)
\end{aligned} \tag{5.21}$$

In this way the stress terms are reduced to source terms that are introduced to the steady-state equations, turning these equations into mean-valued ones. The perturbation equations are formed by subtracting the mean equations from the instantaneous equations. What results are equations that closely resemble the LEE except now the linearization is based on the mean solution instead of the steady state.

5.2 Boundary Conditions

The same procedure used to expand and then time-average the mean equations is applied to the mean boundary conditions. At the inlet the density, pressure, and Mach number are used to expand the boundary conditions starting with the following for density

$$\overline{\frac{\rho_0}{\overline{\rho}+\widetilde{\rho}}} = \overline{\left[1+\frac{\gamma-1}{2}(\overline{M}+\widetilde{M})\right]^{\frac{1}{\gamma-1}}} \tag{5.22}$$

eventually yielding

$$\overline{\rho} = \rho_0\left(1+\frac{\overline{\widetilde{\rho}^2}}{\overline{\rho}^2}\right)\left[\left(1+\frac{\gamma-1}{2}\overline{M}^2\right)^{\frac{1}{\gamma-1}} + \frac{1}{2}\overline{M}\left(\frac{2-\gamma}{\gamma-1}\right)\left(1+\frac{\gamma-1}{2}\overline{M}^2\right)^{\frac{3-2\gamma}{\gamma-1}}\overline{\widetilde{M}^2}\right]^{-1} \tag{5.23}$$

Expanding the pressure condition using

$$\overline{\frac{p_0}{\overline{p}+\widetilde{p}}} = \overline{\left[1+\frac{\gamma-1}{2}(\overline{M}+\widetilde{M})\right]^{\frac{\gamma}{\gamma-1}}} \tag{5.24}$$

yields

$$\overline{p} = p_0\left(1+\frac{\overline{\widetilde{p}^2}}{\overline{p}^2}\right)\left[\left(1+\frac{\gamma-1}{2}\overline{M}^2\right)^{\frac{\gamma}{\gamma-1}} + \frac{1}{2}\overline{M}\left(\frac{\gamma}{\gamma-1}\right)\left(1+\frac{\gamma-1}{2}\overline{M}^2\right)^{\frac{2-\gamma}{\gamma-1}}\overline{\widetilde{M}^2}\right]^{-1} \tag{5.25}$$

For the inlet the mean mass flux $\overline{W}_2$ is extrapolated from the interior cells. The two other conserved flow variables are given by

$$\overline{W}_1 = \overline{\rho} A \tag{5.26}$$

$$\overline{W}_3 = \left(\overline{\rho}\overline{E} + \overline{\widetilde{\rho}\widetilde{E}} \right) A \tag{5.27}$$

At the outlet the mean pressure is specified to be equal to the steady-state pressure and $\overline{W}_1$ and $\overline{W}_2$ are extrapolated from the interior cells. The primitive variables and other flow quantities proceed as already given.

5.3 Numerical Method for NLH

5.3.1 Computational Details

Because of the increased number of computations in the NLH method as compared to the LEE method, a few additional convergence acceleration techniques are used. Pseudo-time marching is achieved again by using the following form for the mean equations where a pseudo-time derivative is introduced

$$\frac{\partial}{\partial \tau} \int_{\Delta x} \overline{W} dx + \oint d\overline{F} = \int_{\Delta x} \overline{S} dx \tag{5.28}$$

The semi-discrete form of the mean equation is given by the following at the j^{th} cell

$$\frac{d}{dt} \left(\overline{W}_j \right) + \frac{1}{\Delta x} (\overline{Q}_j - \overline{D}_j) = \overline{S}_j \tag{5.29}$$

where the net mean-flux $\overline{Q}_j$, the mean dissipative-flux $\overline{D}_j$, and the mean source-term $\overline{S}_j$ are evaluated using what was done in subsection 2.4.2 except now the steady quantities are replaced by the mean-valued ones. The CFL condition is given by the same equation used by the steady state (equation (2.19)) except now the maximum wave speed is found using mean velocity and speed of sound. In order to maximize the CFL number for a given explicit integration scheme, the spatial smoothing of residuals is widely accepted as an important step. Implicit residual-smoothing is used for the mean and perturbation equations to improve the stability of the scheme and the rate of convergence [20, 14]. The central-implicit residual-smoothing is given by

$$-\epsilon Res^*_{j-1} + (1 + 2\epsilon)\, Res^*_j - \epsilon Res^*_{j+1} = Res_j \tag{5.30}$$

where the smoothed residual of the j^{th} cell is Res^*_j and the smoothing parameter is ϵ. This implicit equation of Res^*_j is solved over the whole interior domain using a tri-diagonal-matrix solver.

5.3.2 NLH Procedure

The steps outlined in the Literature Review (section 1.2.3) were quite basic and more details for the NLH method are given below.

1. Steady-state solution to convergence (used as initial condition for mean equations)
2. LEE to convergence (used to form initial condition for perturbation equations)
3. Evaluate stress terms using current perturbation solution (equations (5.7), (5.9), (5.12))
4. Mean equation of NLH iterated one pseudo-time step
5. Perturbation equation of NLH iterated one pseudo-time step

6. Repeat (3) through (5) until convergence of mean and perturbations

5.4 NLH Results and Discussion

The results for the NLH are focused on the transonic cases, where the coupling of mean and perturbation equations has the most impact on accuracy. The residual histories now include the real and imaginary contributions for the perturbation equations and the residuals for the mean equation as well. Using the converged LEE solutions as the initial conditions proved to be troublesome because of the artificially high gradients imposed on the solutions within the first few coupled iterations. For this reason, some of the higher amplitude cases use a modified initial condition that slowly transitions from the LEE solutions to their natural forms, avoiding the extreme gradients that would have caused the solution to diverge. The complex pressure is presented both in first harmonic and mean forms where the NLH has made considerable improvements for the higher amplitude cases (see figures 5.5 and 5.8). Representing the mean solution better was identified as a way to improve the accuracy of the perturbations over the LEE method and the improvement the NLH method provides is evident in figures 5.6 and 5.9. The NLH method does not make any improvements to the highest reduced frequency cases ($\kappa = 10.0$) for the reasons given below. The NLH method improves the accuracy of the cases that present the most non-linear effects with respect to the mean solution and those cases with non-linear effects to the first harmonic are still not so well predicted. Normalized quantities presented include the normalized complex-pressure ($\frac{p'}{\Delta p_b}$), the normalized mean-pressure ($\frac{\bar{p}}{p_0}$), and the normalized residual ($\frac{\frac{1}{N}\Sigma(Res)}{W_{steady}}$).

5.4.1 Subsonic NLH Result

The following subsonic results are presented to highlight the inability of the NLH method to improve the perturbations when either the mean and steady-state solutions are equivalent or when the perturbation itself can no longer be considered to behave linearly. This is true of the subsonic cases that were not captured well with the LEE method. In figure 5.3 the mean solution for the case with the highest level of unsteadiness (reduced frequency and back-pressure amplitude) shows no improvement from the LEE. Because of the non-linear effects present in the first harmonic the results shown in figure 5.2 don't exhibit any improvements in accuracy over the LEE method. For subsonic flows of interest the NLH method does not hold any advantage.

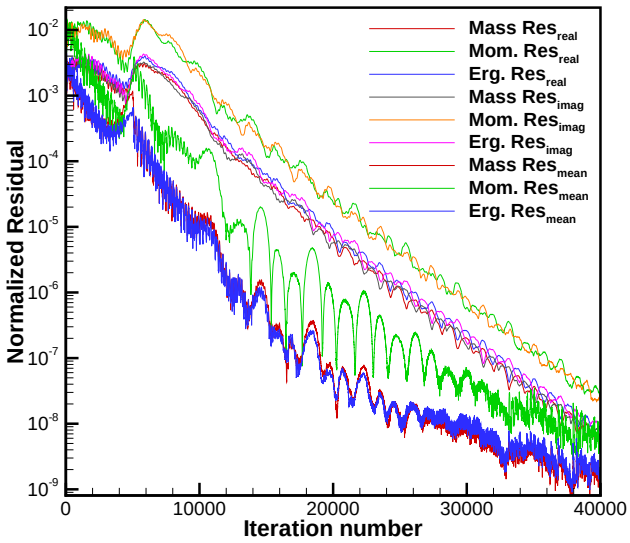

Figure 5.1: NLH transonic residual history at reduced frequency $\kappa = 10.0$, $\frac{\Delta p_b}{p_b} = 5\%$.

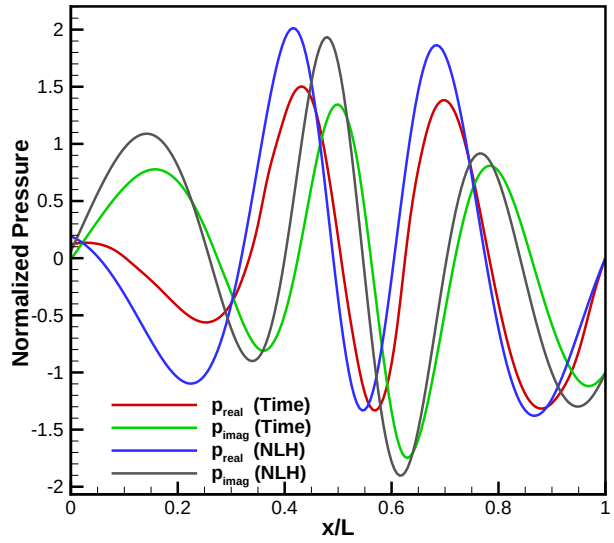

Figure 5.2: NLH transonic results for complex pressure at reduced frequency $\kappa = 10.0$, $\frac{\Delta p_b}{p_b} = 5\%$.

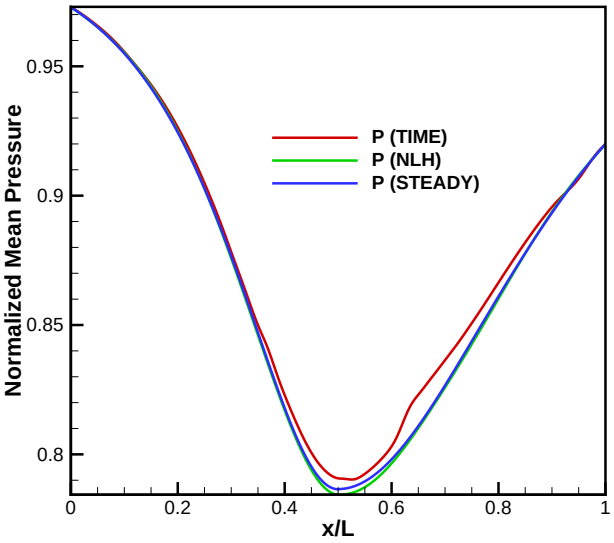

Figure 5.3: NLH transonic mean solution comparison at reduced frequency $\kappa = 10.0$, $\frac{\Delta p_b}{p_b} = 5\%$.

5.4.2 Transonic NLH Results

The CFL number used for the perturbations was 0.6 and for the mean, 2.8. The time-averaged solution near the shock shows considerable smearing when compared to the sharp discontinuity of the steady solution. This smearing increases with increasing back-pressure amplitude and decreasing reduced frequency. An increase in amplitude results in a larger range of motion for the shock and as a result the discontinuity is spread over a larger region. An increase in reduced frequency results in a shorter period of oscillation and more importantly a larger oscillation-period-to-residence-time ratio. This means that when the reduced frequency is significantly larger than the residence time of the fluid particles, the fluid itself cannot respond fast enough to the changing back-pressure conditions and instead lags the boundary condition. When this effect is periodically repeated the lagging response of the fluid results in a shock wave that is very quickly moving but confined to a small range of motion.

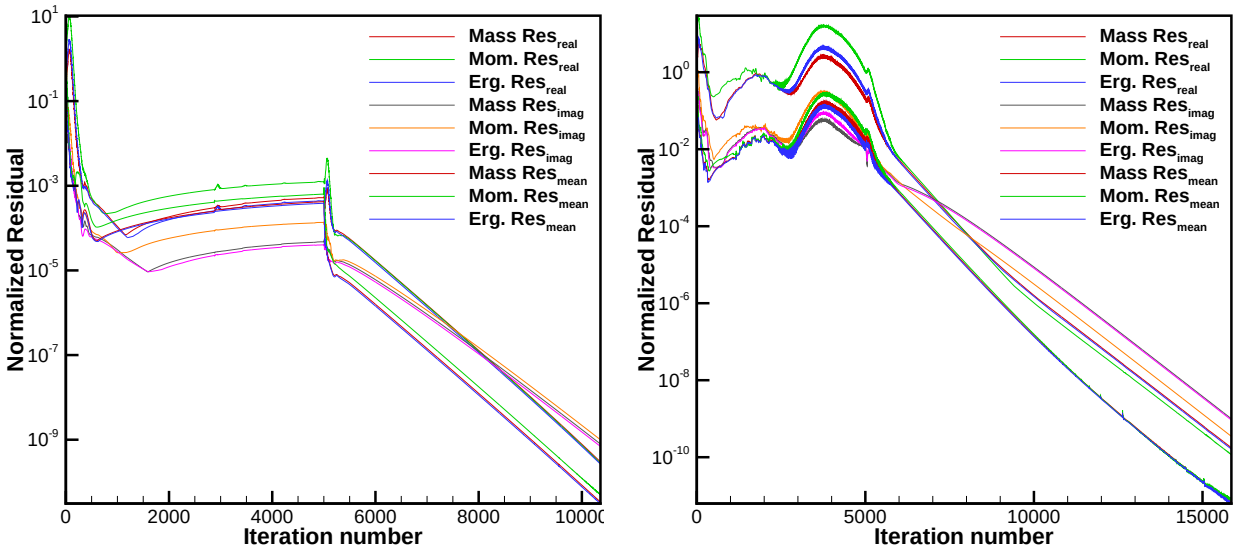

(a) $\frac{\Delta p_b}{p_b} = 0.5\%$ (b) $\frac{\Delta p_b}{p_b} = 5\%$

Figure 5.4: NLH transonic residual history at reduced frequency $\kappa = 0.1$.

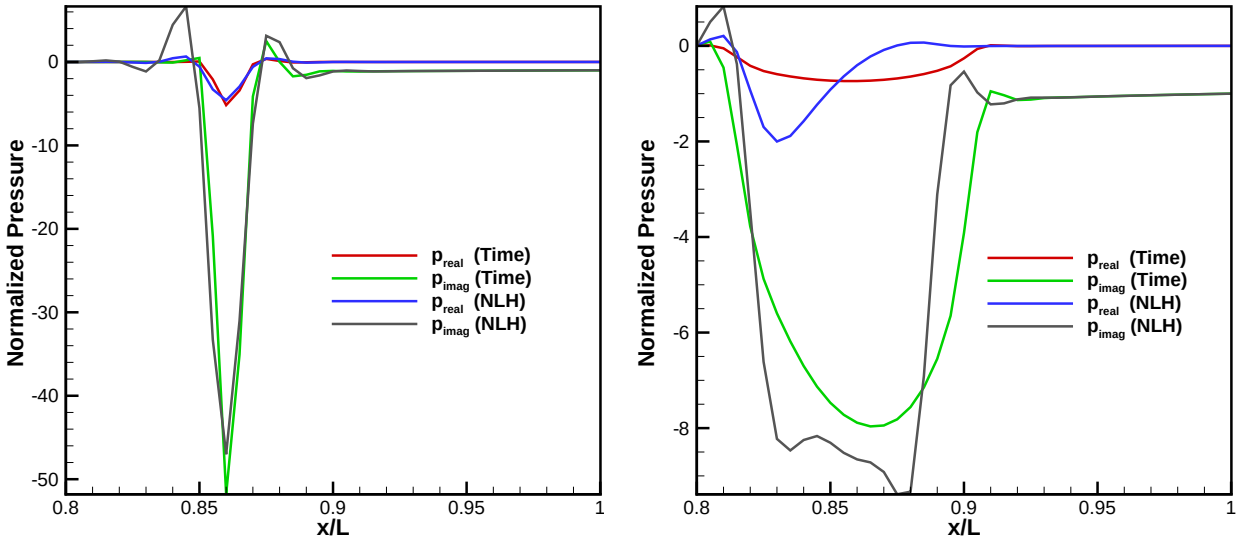

(a) $\frac{\Delta p_b}{p_b} = 0.5\%$ (b) $\frac{\Delta p_b}{p_b} = 5\%$

Figure 5.5: NLH transonic results for complex pressure at reduced frequency $\kappa = 0.1$.

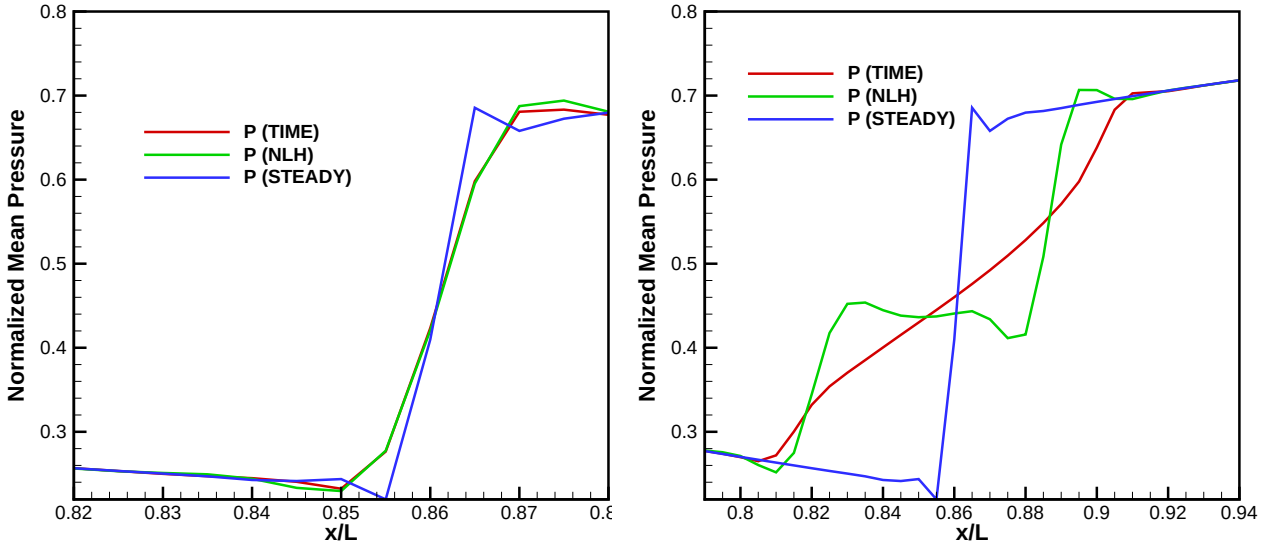

(a) $\frac{\Delta p_b}{p_b} = 0.5\%$ (b) $\frac{\Delta p_b}{p_b} = 5\%$

Figure 5.6: NLH transonic mean solution comparison at reduced frequency $\kappa = 0.1$.

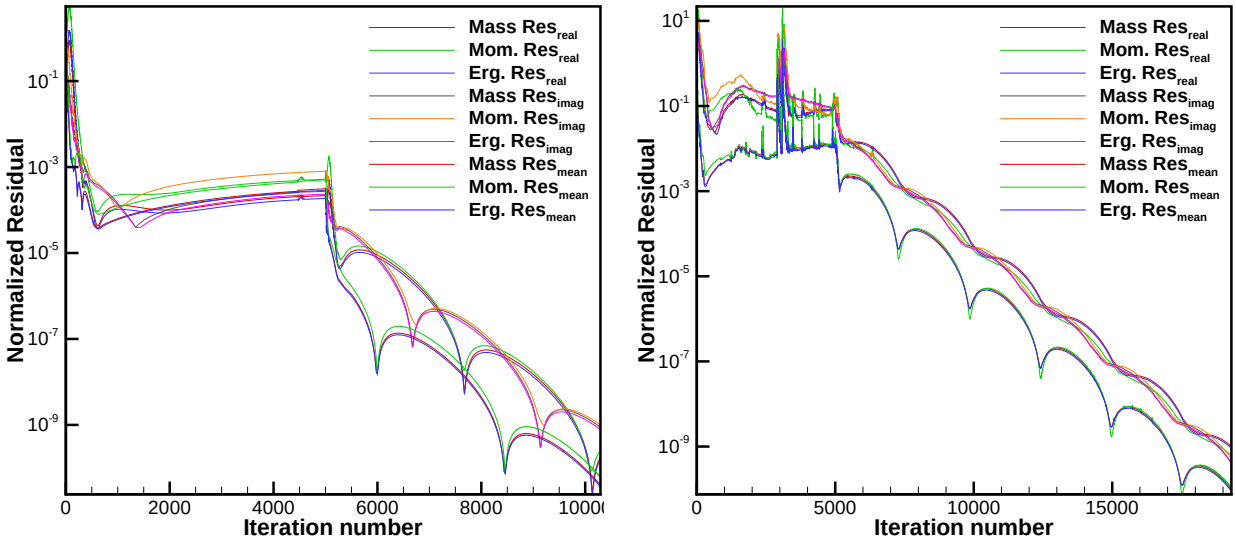

(a) $\frac{\Delta p_b}{p_b} = 0.5\%$ (b) $\frac{\Delta p_b}{p_b} = 5\%$

Figure 5.7: NLH transonic residual history at reduced frequency $\kappa = 1.0$.

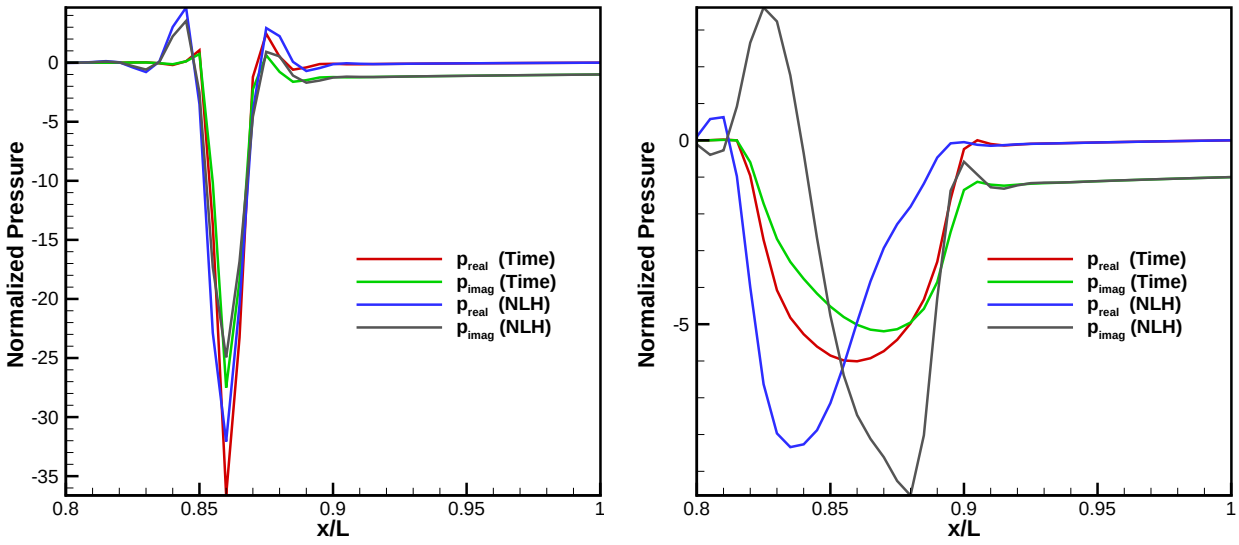

(a) $\frac{\Delta p_b}{p_b} = 0.5\%$ (b) $\frac{\Delta p_b}{p_b} = 5\%$

Figure 5.8: NLH transonic results for complex pressure at reduced frequency $\kappa = 1.0$.

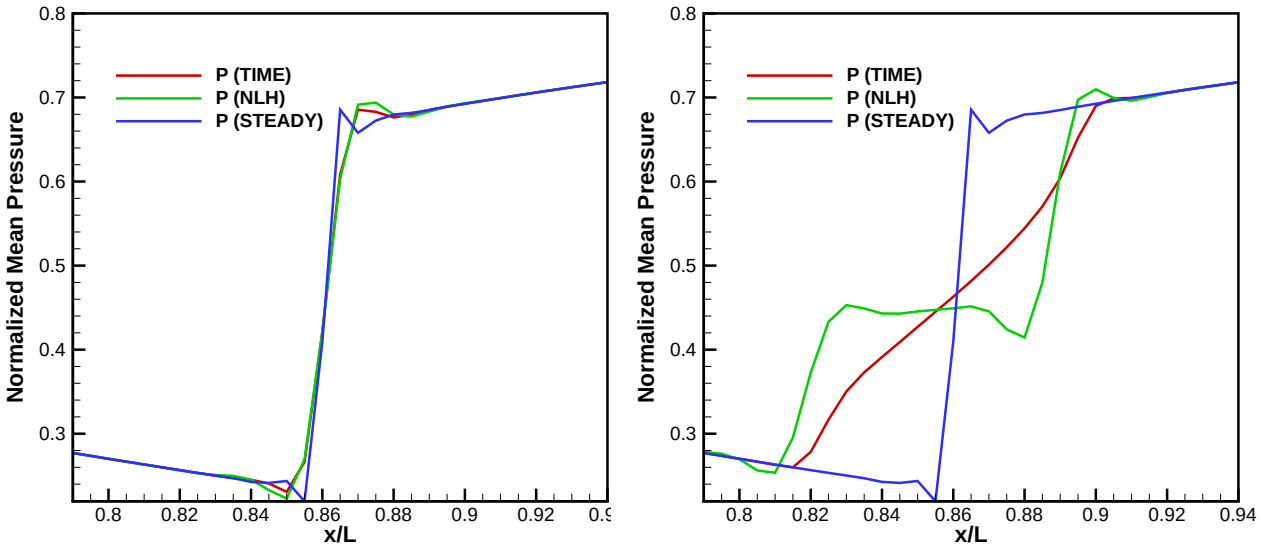

(a) $\frac{\Delta p_b}{p_b} = 0.5\%$ (b) $\frac{\Delta p_b}{p_b} = 5\%$

Figure 5.9: NLH transonic mean solution comparison at reduced frequency $\kappa = 1.0$.

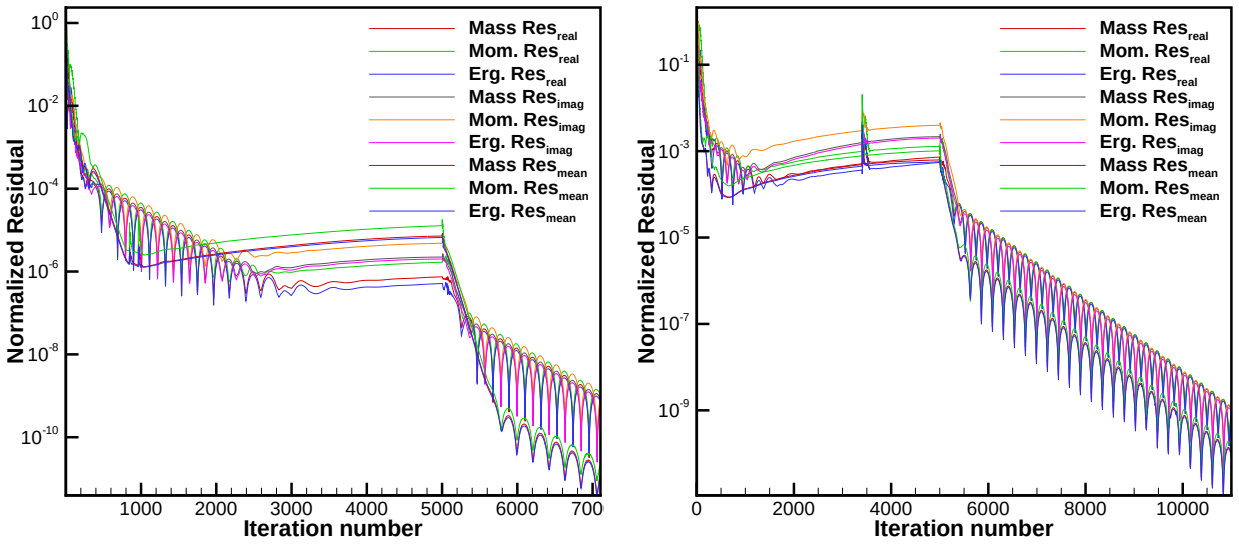

(a) $\frac{\Delta p_b}{p_b} = 0.5\%$ (b) $\frac{\Delta p_b}{p_b} = 5\%$

Figure 5.10: NLH transonic residual history at reduced frequency $\kappa = 10.0$.

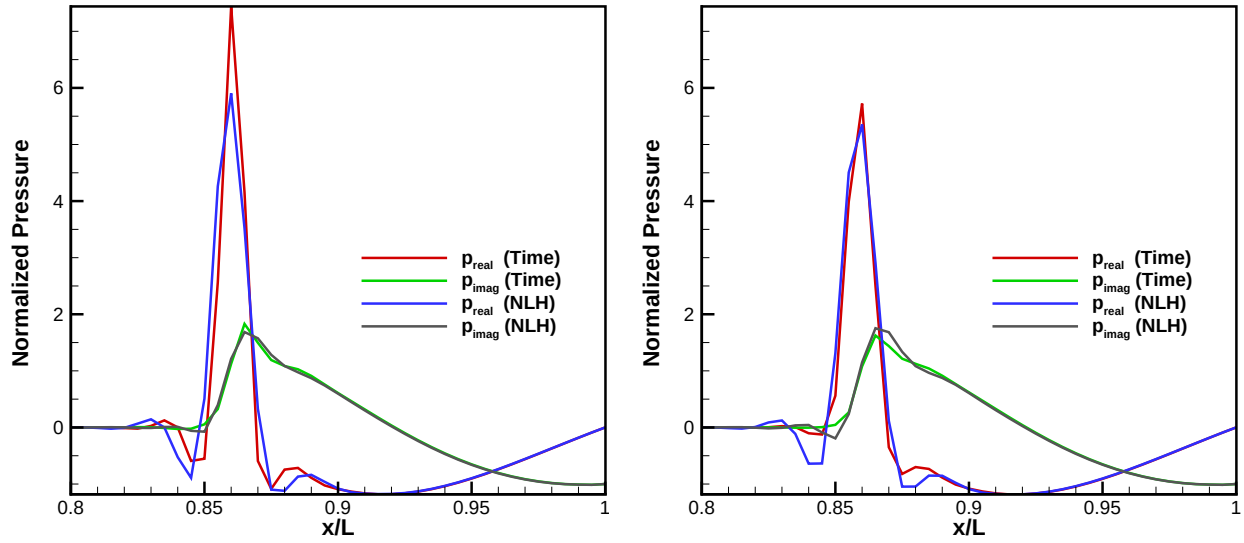

(a) $\frac{\Delta p_b}{p_b} = 0.5\%$ (b) $\frac{\Delta p_b}{p_b} = 5\%$

Figure 5.11: NLH transonic results for complex pressure at reduced frequency $\kappa = 10.0$.

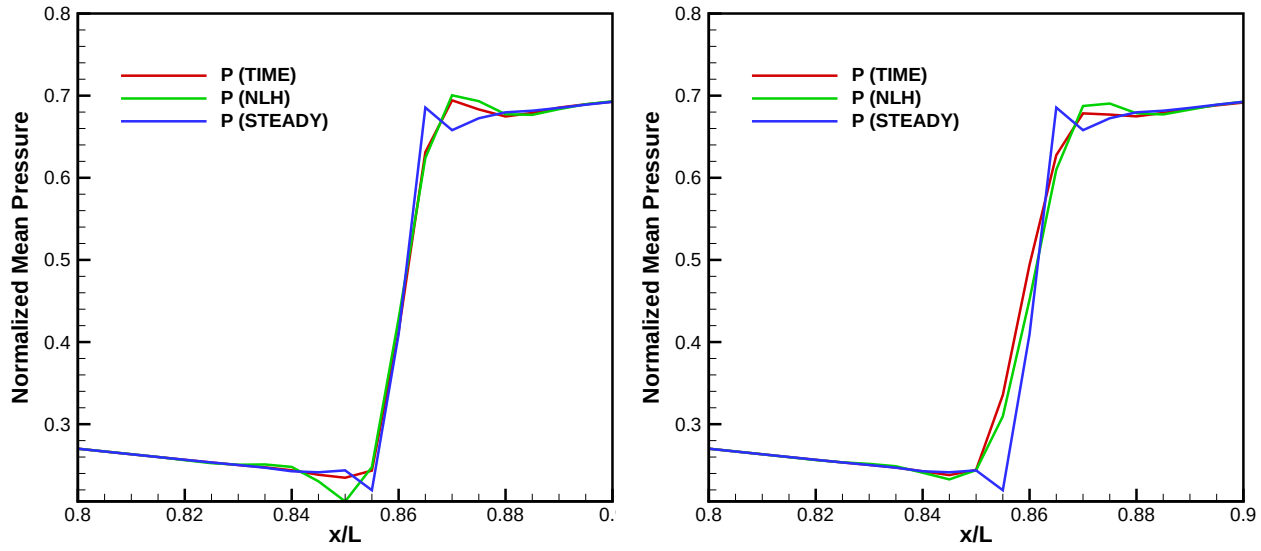

(a) $\frac{\Delta p_b}{p_b} = 0.5\%$ (b) $\frac{\Delta p_b}{p_b} = 5\%$

Figure 5.12: NLH transonic mean solution comparison at reduced frequency $\kappa = 10.0$.

5.5 Transonic Similarity Rule

The transonic results previously presented serve as a parametric study of both the reduced frequency, κ, and the back-pressure amplitude, $\frac{\Delta p_b}{p_b}$. In order to quantify the practicality of using either the LEE or the NLH methods, a transonic similarity rule of said parameters is established. This similarity rule is only with respect to the pressure perturbation which is of particular interest in aeroelastic studies. The normalized pressure-perturbation is proposed to be proportional to the product of two functions as follows

$$\frac{p'}{\Delta p_b} \propto f_1(\kappa) f_2\left(\frac{\Delta p_b}{p_b}\right) \tag{5.31}$$

where f_1 is a function of κ and f_2 is a function of $\frac{\Delta p_b}{p_b}$. The two-norm of the normalized pressure-perturbation serves as the basis for comparing the accuracy of the methods. The average value of the two-norm is given as

$$\Delta p_m = \frac{1}{N}\left\|\frac{p'}{\Delta p_b}\right\|_2 = \frac{1}{N}\left[\sum_{i=0}^{N}(p_i')^2\right]^{\frac{1}{2}} \tag{5.32}$$

The proposed form of the transonic similarity rule is given as

$$\Delta p_m = \frac{A}{1 + B\kappa^C} \tag{5.33}$$

where the expansion of the coefficient A is given to be

$$\begin{aligned} A =& A\left(\kappa = 0, \frac{\Delta p_b}{p_b}\right) \\ =& A_0 + A_1\left(\frac{\Delta p_b}{p_b}\right) + A_2\left(\frac{\Delta p_b}{p_b}\right)^2 + \dots \end{aligned} \tag{5.34}$$

The Δp_m quantity is of constant value in the neighborhood of the linear approximation (when κ and $\frac{\Delta p_b}{p_b}$ are very small). In the expansion of A, the first term, A_0, is said to represent the linear effects that all methods have in common. The higher-order terms (corresponding to $A_1, A_2, \ldots$) represent the non-linear effects that differentiate the NLH and the time-accurate methods from the LEE method. In establshing this rule, the effects of both the reduced frequency and the back-pressure amplitude can be quantified and a comparison to the time-accurate solutions can be made. The following plots show Δp_m as a function of κ for various back-pressure amplitudes. Best-fit cuves for each data set are found by using a least-squares approximation of the proposed similarity rule. The coefficients corresponding to each best-fit curve are given in table 5.1.

$\frac{\Delta p_b}{p_b}$ (%):	A:	B:	C:
LEE			
0.1-5	4.97	0.255	1.38
NLH			
0.1	4.90	0.251	1.38
0.2	4.88	0.250	1.38
0.5	4.75	0.243	1.38
1	4.29	0.213	1.38
2	3.28	0.150	1.38
5	2.21	0.0932	1.38
Time-Accurate			
0.1	4.90	0.252	1.38
0.2	4.85	0.249	1.38
0.5	4.39	0.223	1.38
1	3.77	0.191	1.38
2	2.91	0.144	1.38
5	1.97	0.105	1.38

Table 5.1: Curve-fitted coefficients for transonic similarity rule at varied back-pressure amplitudes.

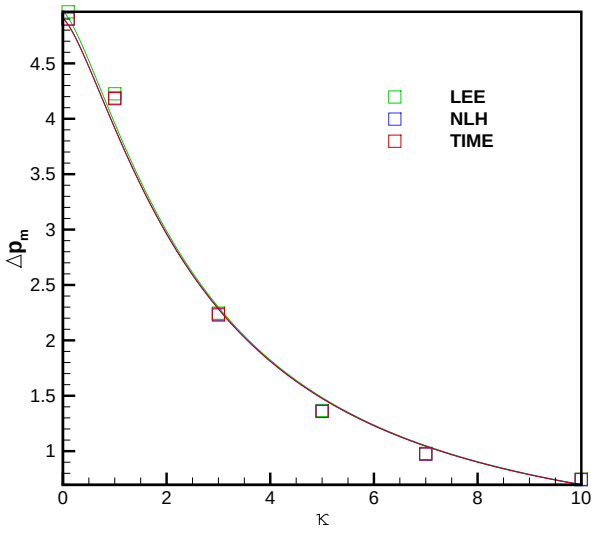

(a) $\frac{\Delta p_b}{p_b} = 0.1\%$

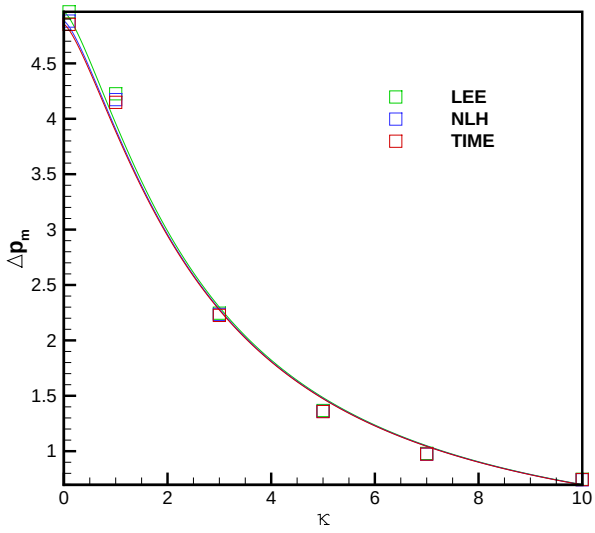

(b) $\frac{\Delta p_b}{p_b} = 0.2\%$

Figure 5.13: Comparison of LEE, NLH, and time-accurate methods for small back-pressure amplitudes.

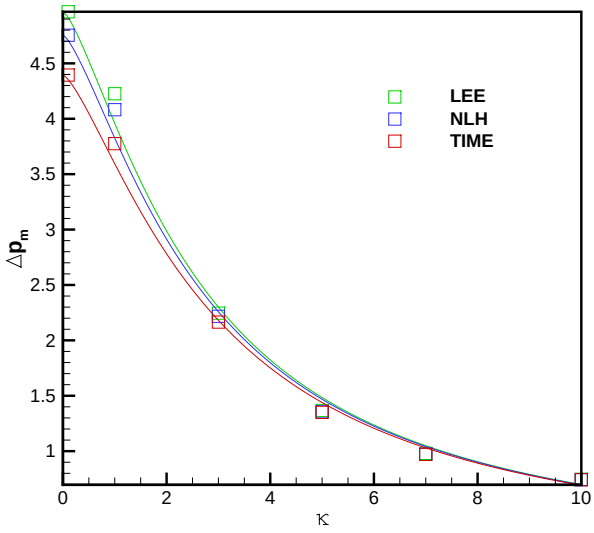

(a) $\frac{\Delta p_b}{p_b} = 0.5\%$

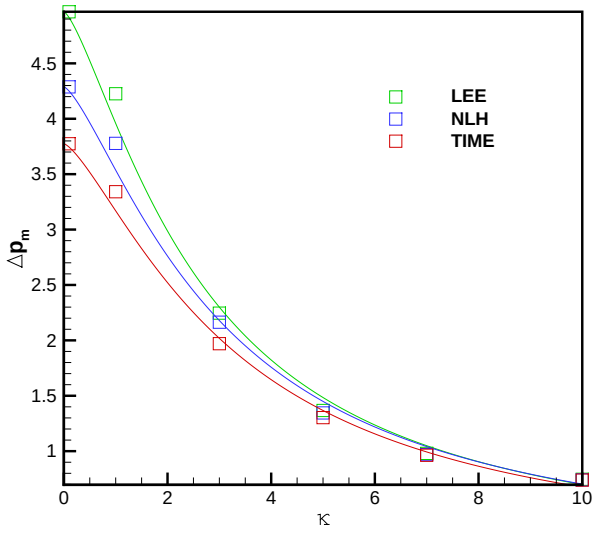

(b) $\frac{\Delta p_b}{p_b} = 1\%$

Figure 5.14: Comparison of LEE, NLH, and time-accurate methods for moderate back-pressure amplitudes.

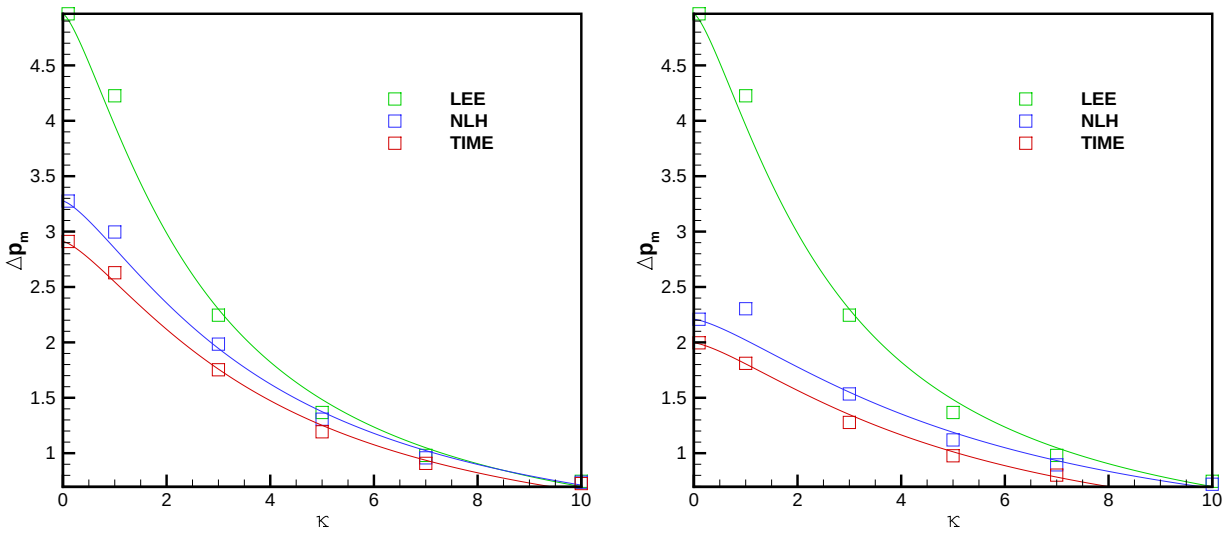

(a) $\frac{\Delta p_b}{p_b} = 2\%$ (b) $\frac{\Delta p_b}{p_b} = 5\%$

Figure 5.15: Comparison of LEE, NLH, and time-accurate methods for large back-pressure amplitudes.

In figure 5.16, a quadratic best-fit is found for Δp_m as a function of back-pressure amplitude (expressed as a percentage). This plot shows the amplitude at varied back-pressures when the reduced frequency is zero. Table 5.2 shows the curve-fitted coefficients for the expansion of A.

	A_0:	A_1:	A_2:
LEE			
	4.97	-	-
NLH			
	5.12	-1.05	0.0933
Time-Accurate			
	5.07	-1.41	0.159

Table 5.2: Curve-fitted coefficients for transonic similarity rule at $\kappa = 0$.

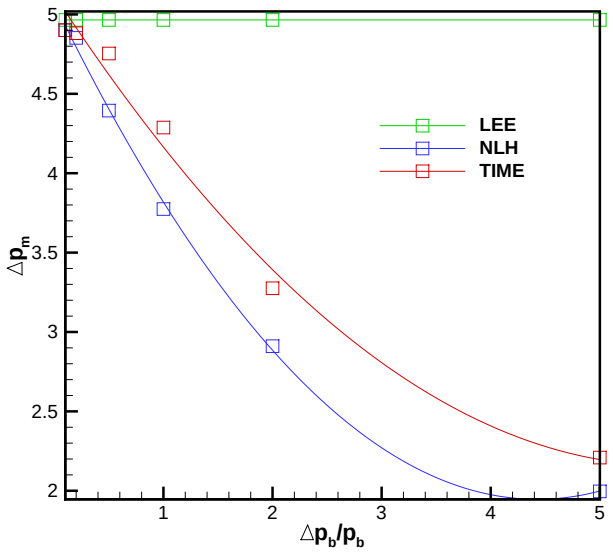

Figure 5.16: Comparison of LEE, NLH, and time-accurate methods for large back-pressure amplitudes.

Overall the LEE method is useful for capturing the perturbation solution when the back-pressure amplitude is small or the reduced frequency is large. For the moderate and large back-pressure amplitudes, the NLH method more closely resembles the full time-accurate solutions.

Chapter 6

Conclusion

6.1 Summary

The linearized Euler equations method and the non-linear harmonic method were both studied under the quasi-1D framework. The LEE method produced accurate predictions for the first harmonic when considering only the small back-pressure amplitude and reduced frequency cases. This limitation is most apparent for the transonic cases which present time-averaged flow fields that differ significantly from the steady-state. The NLH method strives to improve both the mean solution and the first harmonic via the cross coupling of the equations and the introduction of higher-order corrections to the mean. As a whole, the accuracy of the transonic cases was improved greatly yet some limitations still exist. For flows in which the first harmonic is effected by significant non-linearities, the NLH does not produce much better results than the LEE would on the same mean flow. Therefore, the NLH method should be used on transonic cases of low to moderate reduced frequency and back-pressure amplitude.

6.2 Future Work and Recommendations

The primary goal of understanding these harmonic methods and linearized equations has largely been achieved through the work presented. Further application of these methods to the 2D and 3D transonic flutter problems will be initially guided by the findings from this study. Using the LEE and the NLH methods for the flutter problem should yield similar trends and results. Another case to be explored is that of a viscous fluid which means that the Navier-Stokes equations will be used instead of the Euler ones. The motivation for this viscous study is twofold; the study serves to better represent actual flow fields but also serves the purpose of identifying the effects of the shock thickness on the linearized predictions. In the viscous case, the shock is not a simple discontinuity and instead has finite thickness meaning that the linearization occurs on a smoother base solution possibly leading to better results. It will also be of benefit to explore other harmonic methods or variations introduced by Giles, Hall, and He to try and tailor the method specifically for the flutter problem.

Bibliography

[1] Imregun, M., "Prediction of Flutter Stability Using Aeroelastic Frequency Response Functions," *Journal of Fluids and Structures*, Vol. 9, 1995.

[2] Verdon, J. M., "Linearized Unsteady Aerodynamics for Turbomachinery Aeroelastic Applications," *Proceedings of the Twenty-Sixth Joint Propulsion Conference*, AIAA, Washington, DC, 1990.

[3] Hall, K. C., *A Linearized Euler Analysis of Unsteady Flows in Turbomachinery*, Ph.D. thesis, Massachusetts Institute of Technology, 1987.

[4] Hall, K. C. and Crawley, E. F., "Calculation of Unsteady Flows in Turbomachinery Using the Linearized Euler Equations," *AIAA Journal*, Vol. 27, No. 6, 1989.

[5] Lindquist, D. R., *Computation of Unsteady Transonic Flowfields Using Shock Capturing and the Linear Perturbation Euler Equations*, Ph.D. thesis, Massachusetts Institute of Technology, 1992.

[6] Lindquist, D. R. and Giles, M. B., "On the Validity of Linearized Unsteady Euler Equations with Shock Capturing," *Proceedings of the Tenth Computational Fluid Dynamics Conference*, AIAA, Washington, DC, 1991, pp. 800–813.

[7] Giles, M. B., "Analysis of the Accuracy of Shock-Capturing in the Steady Quasi-1D Euler Equations," *Computational Fluid Dynamics Journal*, Vol. 5, No. 2, 1996.

[8] Ning, W. and He, L., "Computation of Unsteady Flows Around Oscillating Blades Using Linear and Nonlinear Harmonic Euler Methods," *Journal of Turbomachinery*, Vol. 120, 1998, pp. 508–514.

[9] Hall, K. C., Thomas, J. P., and Clark, W. S., "Computation of Unsteady Nonlinear Flows in Cascades Using a Harmonic Balance Technique," *AIAA Journal*, Vol. 40, No. 5, 2002, pp. 879–886.

[10] Giles, M. B., "A Framework for Multi-Stage Unsteady Flow Calculations," *Proceedings of the Sixth International Symposium on Unsteady Aerodynamics, Aeroacoustics and Aeroelasticity of Turbomachines and Propellers*, Springer-Verlag, 1991, pp. 57–72.

[11] He, L. and Ning, W., "Efficient Approach for Analysis of Unsteady Viscous Flows in Turbomachines," *AIAA Journal*, Vol. 36, No. 11, 1998, pp. 2005–2012.

[12] Giles, M. B., "Nonreflecting Boundary Conditions for Euler Equation Calculations," *AIAA Journal*, Vol. 28, No. 12, 1990, pp. 2050–2058.

[13] Jameson, A., Schmidt, W., and Turkel, E., "Numerical Solution of the Euler Equations by Finite Volume Methods Using Runge Kutta Time Stepping Schemes," *Proceedings of the Fourteenth Fluid and Plasma Dynamics Conference*, AIAA, 1981.

[14] Jameson, A., "Numerical Solution of the Euler Equations for Compressible Inviscid Fluids," 1983, MAE Report no. 1643.

[15] Jameson, A., "Transonic Flow Calculations," MAE Report no. 1651.

[16] Dwight, R. P. and Bijl, H., *Solution Methods and Acceleration Techniques in CFD*, John Wiley and Sons, Ltd., 2010.

[17] Smith, S. W., *The Scientist and Engineer's Guide to Digital Signal Processing*, 1998.

[18] Zhang, Z., Yang, S., and Chen, P. C., "Linearized Euler Solver for Rapid Frequency-Domain Aeroelastic Analysis," *Journal of Aircraft*, Vol. 49, No. 3, 2012, pp. 922–932.

[19] Kreiselmaier, E. and Laschka, B., "Small Disturbance Euler Equations: Efficient and Accurate Tool for Unsteady Load Prediction," *Journal of Aircraft*, Vol. 37, No. 5, 2000, pp. 770–778.

[20] Haelterman, R., Vierendeels, J., and Heule, D. V., "Optimization of the Runge-Kutta Iteration with Residual Smoothing," *Journal of Computational and Applied Mathematics*, 2010, pp. 253–271.